

UC Berkeley

UC Berkeley Previously Published Works

Title

Variability-selected Intermediate-mass Black Hole Candidates in Dwarf Galaxies from ZTF and WISE

Permalink

<https://escholarship.org/uc/item/51r0j5gj>

Journal

The Astrophysical Journal, 936(2)

ISSN

0004-637X

Authors

Ward, Charlotte
Gezari, Suvi
Nugent, Peter
[et al.](#)

Publication Date

2022-09-01

DOI

10.3847/1538-4357/ac8666

Copyright Information

This work is made available under the terms of a Creative Commons Attribution License, available at <https://creativecommons.org/licenses/by/4.0/>

Peer reviewed



Variability-selected Intermediate-mass Black Hole Candidates in Dwarf Galaxies from ZTF and WISE

Charlotte Ward^{1,2}, Suvi Gezari^{1,3}, Peter Nugent^{2,4}, Eric C. Bellm⁵, Richard Dekany⁶, Andrew Drake⁷, Dmitry A. Duev⁷, Matthew J. Graham⁷, Mansi M. Kasliwal⁷, Erik C. Kool⁸, Frank J. Masci⁹, and Reed L. Riddle⁷

¹Department of Astronomy, University of Maryland, College Park, MD 20742, USA; charlotteward@astro.umd.edu

²Lawrence Berkeley National Laboratory, 1 Cyclotron Road, Berkeley, CA 94720, USA

³Space Telescope Science Institute, 3700 San Martin Dr., Baltimore, MD 21218, USA

⁴Department of Astronomy, University of California, Berkeley, Berkeley, CA 94720, USA

⁵DIRAC Institute, Department of Astronomy, University of Washington, 3910 15th Avenue NE, Seattle, WA 98195, USA

⁶Caltech Optical Observatories, California Institute of Technology, Pasadena, CA 91125, USA

⁷Division of Physics, Mathematics, and Astronomy, California Institute of Technology, Pasadena, CA 91125, USA

⁸The Oskar Klein Centre, Department of Astronomy, Stockholm University, AlbaNova, SE-10691, Stockholm, Sweden

⁹IPAC, California Institute of Technology, 1200 E. California Blvd, Pasadena, CA 91125, USA

Received 2021 October 26; revised 2022 July 14; accepted 2022 August 1; published 2022 September 6

Abstract

While it is difficult to observe the first black hole seeds in the early universe, we can study intermediate-mass black holes (IMBHs) in local dwarf galaxies for clues about their origins. In this paper we present a sample of variability-selected active galactic nuclei (AGN) in dwarf galaxies using optical photometry from the Zwicky Transient Facility (ZTF) and forward-modeled mid-IR photometry of time-resolved Wide-field Infrared Survey Explorer (WISE) co-added images. We found that 44 out of 25,714 dwarf galaxies had optically variable AGN candidates and 148 out of 79,879 dwarf galaxies had mid-IR variable AGN candidates, corresponding to active fractions of $0.17\% \pm 0.03\%$ and $0.19\% \pm 0.02\%$, respectively. We found that spectroscopic approaches to AGN identification would have missed 81% of our ZTF IMBH candidates and 69% of our WISE IMBH candidates. Only nine candidates have been detected previously in radio, X-ray, and variability searches for dwarf galaxy AGN. The ZTF and WISE dwarf galaxy AGN with broad Balmer lines have virial masses of $10^5 M_\odot < M_{\text{BH}} < 10^7 M_\odot$, but for the rest of the sample, BH masses predicted from host galaxy mass range between $10^{3.2} M_\odot < M_{\text{BH}} < 10^{7.25} M_\odot$. We found that only 5 of 152 previously reported variability-selected AGN candidates from the Palomar Transient Factory in common with our parent sample were variable in ZTF. We also determined a nuclear supernova fraction of $0.05\% \pm 0.01\% \text{ yr}^{-1}$ for dwarf galaxies in ZTF. Our ZTF and WISE IMBH candidates show the promise of variability searches for the discovery of otherwise hidden low-mass AGN.

Unified Astronomy Thesaurus concepts: Active galactic nuclei (16); Intermediate-mass black holes (816); Dwarf galaxies (416)

1. Introduction

It is challenging to determine how the very first massive black holes (BHs) formed because they have grown over time as galaxies merge and their BHs accrete (Volonteri & Begelman 2010). High-redshift BH seeds are very difficult to detect owing to their low luminosities (Volonteri & Reines 2016), so we can instead constrain models of BH seed formation by studying the least massive BHs in local galaxies (Reines & Comastri 2016). These low-mass analogs to BH seeds are called intermediate-mass BHs (IMBHs) and have masses in the range $100 M_\odot < M_{\text{BH}} < 10^6 M_\odot$. Dwarf galaxies of stellar mass $M_* < 10^{9.75} M_\odot$ are the best place to find low-mass BHs because galaxy mass and BH mass are correlated (e.g., Kormendy & Ho 2013; Woo et al. 2013). Supernova (SN) driven stunting of BH growth in dwarf galaxies also makes these BHs comparable to early BH seeds (Habouzit et al. 2017; Anglés-Alcázar et al. 2017).

The low-mass end of galaxy population relations such as the BH occupation fraction and the slope and scatter of the relationship between BH mass and the stellar velocity

dispersion of the host bulge ($M_{\text{BH}-\sigma_*}$; Ferrarese & Merritt 2000) will vary depending on the formation mechanism of early BH seeds (see Greene et al. 2020, for a review). For example, Population III stars will produce a population of undermassive BHs in low-redshift galaxies with stellar dispersion $\sigma_* < 100 \text{ km s}^{-1}$, while direct collapse mechanisms will produce heavier BHs, resulting in a flattening of the $M_{\text{BH}-\sigma}$ relation around masses of $10^5 M_\odot$ (Volonteri & Natarajan 2009). Although the potential for low-mass BH populations to constrain BH seed formation histories may be limited by uncertainties in accretion prescriptions (Ricarte & Natarajan 2018), it nonetheless motivates the discovery of a large population of BHs in low-mass galaxies. A recent effort by Baldassare et al. (2020a) to fill in the low-mass end of the $M_{\text{BH}-\sigma_*}$ relation doubled the number of BHs with measured virial masses and stellar velocity dispersions in dwarf galaxies of $M_* < 3 \times 10^9 M_\odot$ to 15, and the results were in agreement with an extrapolation of the linear relationship observed for high-mass galaxies. However, larger numbers of low-mass AGN, particularly in galaxies of mass $M_* < 3 \times 10^8$, are needed to more fully constrain seed models.

The fraction of IMBHs in dwarf galaxies that are wandering in their galaxy halos, rather than occupying the nucleus, may also constrain BH seed formation mechanisms. The wandering fraction is dependent on galaxy merger history but will be



Original content from this work may be used under the terms of the [Creative Commons Attribution 4.0 licence](https://creativecommons.org/licenses/by/4.0/). Any further distribution of this work must maintain attribution to the author(s) and the title of the work, journal citation and DOI.

substantially higher if massive BHs were produced by gravitational runaway of massive-star remnants (Miller & Hamilton 2002; Portegies Zwart & McMillan 2002) due to the high frequency of IMBH ejection during these interactions (Volonteri & Perna 2005; Holley-Bockelmann et al. 2008). Ricarte et al. (2021) found that a substantial population of wandering BHs exist in the ROMULUS cosmological simulations and make up 10% of BH mass in the local universe. Studies of IMBHs of mass $3.8 < \log M_{\text{BH}}(M_{\odot}) < 7.0$ in cosmological zoom-in simulations suggest that 50% of IMBHs in dwarf galaxies are wandering within 7 kpc of the galaxy center owing to historical galaxy mergers (Bellovary et al. 2018, 2021). This is supported by radio observations of dwarf galaxy AGN (Reines et al. 2020). Observational constraints on the wandering fraction of IMBHs in dwarf galaxies will help to test the accuracy of cosmological merger simulations, the effects of gravitational wave recoil on BHs in low-mass galaxies, and the feasibility of the gravitational runaway BH seed formation mechanism.

A major challenge both for the search for IMBHs and for estimating the occupation and wandering fractions is that the predicted accretion rates are very low, particularly for nonnuclear AGN. BH accretion may be bimodal in its efficiency, causing low-mass BHs $< 10^5 M_{\odot}$ to grow more slowly (Pacucci et al. 2018). Bellovary et al. (2018) found that most simulated IMBHs reach a maximum bolometric luminosity of $\log L_{\text{bol}}(\text{erg s}^{-1}) < 41$ and are therefore very difficult to detect. Pacucci et al. (2021) used a theoretical model based on galaxy mass and the angular momentum available in nuclear regions to estimate an active fraction of 5%–22% of AGN in dwarf galaxies, which increases with host mass. The level of activity likely depends on the merger history of the dwarf galaxy. Kristensen et al. (2021) find that inactive dwarf galaxies in the Illustris simulations tend to have been residing in dense environments for long times, while active galaxies had commonly been in a recent (≤ 4 Gyr) minor merger.

Discovery of AGN activity in dwarf galaxies will also help us to test predictions on the importance of AGN feedback in the low-mass regime. While Geha et al. (2012) found that dwarf galaxies in the Sloan Digital Sky Survey (SDSS) with no active star formation are extremely rare and that more massive neighboring galaxies were the cause of star formation quenching, Penny et al. (2018) and Dickey et al. (2019) have found evidence for internal AGN-driven quenching in a small number of dwarf galaxies. Simulations suggest that dwarf galaxies hosting overmassive BHs have lower central stellar mass density, lower H I gas content, and lower star formation rates than dwarf galaxies with undermassive counterparts, suggesting that internal feedback in dwarf galaxies can quench star formation only for higher-mass BHs (Sharma et al. 2019). Simulations by Koudmani et al. (2019) found that AGN outflows in dwarf galaxies only have a small effect on regulating global star formation rates compared to SNe and sustained high-luminosity AGN with isotropic winds.

Detailed observational studies of small dwarf galaxy samples have painted a different picture. GMOS IFU observations of eight dwarf galaxies by Liu et al. (2020) discovered the presence of high-velocity outflows in seven out of eight, with some outflows capable of expelling a portion of outflowing material from the galaxy and enriching the surrounding circumgalactic medium. Coronal line emission inconsistent

with shocks was also detected from five of these objects (Bohn et al. 2021). Larger samples of AGN in dwarf galaxies will allow for further searches for signatures of AGN feedback such as high-velocity and large-scale outflows.

A range of approaches have been used to obtain samples of AGN candidates in dwarf galaxies. Some studies have taken a spectroscopic approach by looking for the emission-line signatures of AGN in low-mass galaxies. Reines et al. (2013) found that 151 dwarf galaxies with masses $10^{8.5} M_{\odot} < M_{*} < 10^{9.5} M_{\odot}$ among a sample of 25,000 had [O III] $\lambda 5007/\text{H}\beta$ and [N II] $\lambda 6550/\text{H}\alpha$ narrow emission line ratios indicative of AGN activity. Mezcuca & Domínguez Sánchez (2020) found a sample of 37 dwarf galaxies with “hidden” AGN ionization lines by spatially resolving emission from star-forming regions and nuclear AGN within each dwarf galaxy using MaNGA integral field unit spectroscopy. Molina et al. (2021) used [Fe X] $\lambda 6374$ coronal line emission as a signature of AGN accretion to find 81 dwarf galaxies with possible IMBHs.

Multiwavelength approaches have also been successful in the identification of AGN in dwarf galaxies. Mezcuca et al. (2018) identified 40 AGN in dwarf galaxies with stellar masses $10^7 M_{\odot} < M_{*} < 3 \times 10^9 M_{\odot}$ via their X-ray emission in the Chandra COSMOS Legacy Survey, finding an AGN fraction of $\sim 0.4\%$ for redshifts less than 0.3. Reines et al. (2020) found that 39 of 111 dwarf galaxies had compact radio sources at 8–12 GHz with the Karl G. Jansky Very Large Array (VLA) and determined that 13 of these could confidently be classified as AGN. They also found that 10 of the 13 radio AGN detected were spatially offset from their optical galaxy nuclei.

A new approach to the detection of IMBH candidates has been to search for AGN-like stochastic variability from low-mass galaxies as a signature of the presence of a central BH. Baldassare et al. (2018) found 135 galaxies with AGN-like variability on yearly timescales when constructing light curves of $\sim 28,000$ galaxies with SDSS spectra, including 12 from dwarf galaxies with stellar masses $M_{*} < 3 \times 10^9 M_{\odot}$. They therefore estimated a variability fraction of 0.1% for AGN in dwarf galaxies. A similar study in 2020 used light curves from the Palomar Transient Factory (PTF; Law et al. 2009) to search for variable AGN in 35,000 galaxies with stellar mass $M_{*} < 10^{10} M_{\odot}$, identifying variability in 102 galaxies with masses $M_{*} < 3 \times 10^9 M_{\odot}$ (Baldassare et al. 2020b).

As some low-mass AGN vary on hourly timescales, very high cadence surveys have proved effective for the discovery of variability from dwarf galaxy AGN. For example, Burke et al. (2020) produced a 30-minute-cadence, 1-month-long light curve of the AGN in the archetypal dwarf galaxy NGC 4395 using data from the Transiting Exoplanet Survey Satellite (TESS). The $\sim 10^5 M_{\odot}$ BH was variable with a characteristic timescale of $1.4_{-0.5}^{+1.9}$ days. Martínez-Palomera et al. (2020) used data from the HiTS imaging survey, which undertook 1 week of high-cadence (4 times per night) and high-coverage ($120\text{--}150 \text{ deg}^2$) observations with the Dark Energy Camera each year for 3 yr, to search for short-timescale IMBH variability. They identified 500 galaxies with hourly, small-amplitude variation in their week-long light curves. They estimated that 4% of dwarf galaxies contained an IMBH based on their results. Shaya et al. (2015) monitored ~ 500 galaxies with the Kepler telescope (Borucki et al. 2010) and found that while 4% showed bright AGN activity, many other galaxies

exhibited faint (down to 0.001 mag) variability, which may also have been due to the presence of a low-mass AGN.

Recently, Secrest & Satyapal (2020) undertook a search for variable AGN in the mid-IR. This was motivated by the sensitivity of mid-IR studies to low-luminosity AGN that are frequently optically obscured and Compton-thick (Ricci et al. 2016; Annuar et al. 2017) and frequently unobservable in the soft X-rays (Polimera et al. 2018), along with the low contamination rates of SNe due to weak mid-IR emission (Smitka 2016). To produce mid-IR light curves, Secrest & Satyapal (2020) used multiepoch photometry from the Wide-field Infrared Survey Explorer (WISE; Wright et al. 2010). WISE mapped the sky in the W1 (3.4 μm) and W2 (4.6 μm) bands with 6-month cadence over an 8 yr baseline between the initial observations in 2010, the Near-Earth Object Wide-field Infrared Survey Explorer mission from 2010 to 2011 (NEOWISE; Mainzer et al. 2011), and the reactivation mission beginning in 2013 (NEOWISE-R; Mainzer et al. 2014). Secrest & Satyapal (2020) found a sample of 2199 dwarf galaxies of stellar mass $M_* < 2 \times 10^9 M_\odot$ and redshift $0.02 < z < 0.03$ from the NASA-Sloan Atlas, which had corresponding sources in the All WISE catalog. Among this sample, only 2 (0.09%) showed significant variability in light curves produced by the AllWISE Multiepoch Photometry Table and the NEOWISE-R Single Exposure Source Table.

Variability-based search strategies have been particularly good at finding AGN candidates in dwarf galaxies that are optically obscured or unidentifiable by their spectroscopic signatures. For example, only 25% of the optically variable AGN candidates in galaxies of mass $M_* < 10^{10} M_\odot$ found in PTF were classified as AGN or composite galaxies based on their narrow emission lines (Baldassare et al. 2020b). This is likely due to a combination of star formation dilution of AGN emission lines and the hardening of the accretion disk SED around lower-mass BHs that extends the partially ionized zone and reduces the emission-line ratios normally used for AGN classification (Cann et al. 2019). Variability-based strategies therefore have an important place for finding AGN that would otherwise be missed owing to biases in other selection techniques.

Previous searches for active IMBH candidates in dwarf galaxies with spectroscopic, radio, X-ray, and mid-IR observations have not provided a complete, unbiased census of the IMBH occupation fraction because different strategies are hindered by high star formation rates, obscuration and low accretion luminosities. Therefore, despite the discoveries of these large samples of dwarf AGN candidates, there are very few confirmed IMBHs with well-sampled SEDs and measured virial BH masses that we can use to occupy the sparsely populated low-mass ends of a number of BH–galaxy scaling relations. This motivates the development of effective search strategies for identifying substantially larger samples of IMBH candidates. This will provide more opportunities for careful confirmation and multiwavelength characterization of the best candidates, especially those with broad Balmer lines.

In this paper we present a comprehensive search for AGN-like variability from a large sample of dwarf galaxies in the optical and mid-IR in order to build on the previous successes of Baldassare et al. (2018, 2020b) and Secrest & Satyapal (2020) with SDSS, PTF, and WISE. For our optical search we have used observations from the Zwicky Transient Facility (ZTF; Bellm et al. 2019b; Graham et al. 2019; Dekany et al. 2020), a new and ongoing optical survey that began in 2018

March and achieves single-epoch limiting magnitudes of ~ 21 in g , r , and i band over a survey footprint of 23,675 deg^2 . The Northern Sky Survey of ZTF Phase I (2018 March–2020 September) had an average cadence of 3 days, and this was supplemented by higher-cadence subsurveys with hourly to 1-day cadences (Bellm et al. 2019a). The ongoing ZTF Phase II (2020 October–present) Northern Sky Survey has a 2-day cadence. By comparison, PTF had a footprint of $\sim 8000 \text{ deg}^2$ and a ~ 5 -day cadence. To expand on the mid-IR variability search of Secrest & Satyapal (2020), we have made use of new forward-modeled photometry catalogs of time-resolved WISE co-adds to produce more sensitive photometry of a larger dwarf galaxy sample. We do this work in preparation for the upcoming Legacy Survey of Space and Time (LSST) at Vera C. Rubin Observatory (Ivezić et al. 2019), which will provide a more complete census of variable IMBHs over the next decade owing to its expected single-visit limiting magnitude of $g \sim 25$ at a 3-day cadence spanning ~ 10 yr.

In Section 2 we describe our dwarf galaxy sample selection process. In Section 3 we describe our procedure for ZTF forced photometry of the dwarf galaxy sample. In Section 4 we describe our selection strategy for finding the optically variable AGN. In Section 5 we present our sample of IMBH candidates and SNe from ZTF and describe their multiwavelength and spectroscopic properties. In Section 6 we describe our selection of variable AGN in WISE based on forward-modeled photometry of time-resolved co-adds, and in Section 7 we discuss the multiwavelength and spectroscopic properties of the WISE-selected IMBH candidates. In Section 8 we discuss the merits of the two selection strategies and the properties of the IMBH candidates in further depth.

2. Dwarf Galaxy Sample Selection

We selected a sample of dwarf galaxies using the NASA-Sloan Atlas (NSA) version v1.0.1.¹⁰ The NSA produced stellar mass estimates for galaxies by fitting five templates derived from stellar population synthesis models (Bruzual & Charlot 2003; Blanton & Roweis 2007) to SDSS images of galaxies after subtracting the sky background (Blanton et al. 2011). We used this catalog of stellar masses to allow for more direct comparison to other AGN variability searches that classify dwarf galaxies using stellar masses from this catalog (e.g., Reines et al. 2013; Baldassare et al. 2018, 2020b; Secrest & Satyapal 2020).

When compiling our list of dwarf galaxies from the NSA, we required redshifts of $0.02 < z < 0.35$ and elliptical Petrosian masses of $M_* < 3 \times h^{-2} 10^9 M_\odot$. We selected an h value of 0.73 for consistency with Reines et al. (2013) and Secrest & Satyapal (2020) such that our mass cutoff corresponds to $M_* < 10^{9.75} M_\odot$. After finding some high-redshift quasars listed in the catalog with erroneous redshifts and underestimated stellar masses, we required the NSA redshift to be derived from an SDSS spectrum (described by the ZSRC column in the NSA table). This resulted in a final sample of 81,462 dwarf galaxies.

For the ZTF photometry, we also required that the objects overlap with > 100 high-quality g - and r -band ZTF images over a > 1 yr baseline. Due to computational limitations, we selected a random subset of the parent light-curve sample consisting of 25,714 dwarf galaxies for our ZTF variability search. For our WISE variability search we required there to be > 5 epochs

¹⁰ <https://www.sdss.org/dr16/manga/manga-target-selection/nsa>

over a >3 yr baseline, and this resulted in a final sample of 79,879 objects for the mid-IR search.

We produced a control sample of optically variable AGN with host galaxies of mass $M_* > 10^{9.75} M_\odot$ from a parent sample of 5493 variable ZTF AGN found by Ward et al. (2021). This AGN sample was obtained from the ZTF alert stream (Patterson et al. 2019) using the AMPEL alert broker AMPEL (Alert Management, Photometry and Evaluation of Lightcurves; Nordin et al. 2019) to cross-match ZTF transients to AGN catalogs using `catsHTM` (Soumagnac & Ofek 2018) and check for AGN-like variability with the Butler & Bloom (2011) quasar modeling routine. We matched the AGN from this sample to the NASA-Sloan Atlas with a $5''$ radius and found 1,053 objects with measured galaxy masses. Both the control sample and the dwarf galaxy sample were processed by the following photometry pipeline.

3. ZTF Photometry of Dwarf Galaxies

Difference imaging to detect variability requires the production of reference images, which are co-added stacks of exposure images to support image differencing downstream. To produce new ZTF forced photometry with custom, deeper references than the main ZTF alert pipeline, we implemented the ZUDS photometry pipeline¹¹ on our dwarf galaxy and AGN control samples. We generated reference images for each field, CCD, quadrant, and filter from ZTF single-epoch science images by selecting up to 60 images as close as possible in time that met the following criteria established by Masci et al. (2019) for the main ZTF alert pipeline:

1. Seeing within the range $2''.0 \leq \text{FWHM} \leq 5''.0$, with priority given to images with lower seeing values.
2. Quality status = 1.
3. Magnitude zero-points given by $25.3 \leq \text{MAGZP}(g) \leq 26.5$ or $25.3 \leq \text{MAGZP}(r) \leq 26.5$ for filters g and r , respectively.
4. Color coefficients given by $-0.20 \leq \text{CLRCEFF}(g) \leq 0.15$ or $-0.05 \leq \text{CLRCEFF}(r) \leq 0.22$ for filters g and r , respectively.
5. Limiting magnitudes given by $\text{MAGLIM}(g) \geq 19.0$ or $\text{MAGLIM}(r) \geq 19.0$ for filters g and r , respectively.
6. Global pixel median ≤ 1900 DN or ≤ 1600 for filters g and r , respectively.
7. Global robust pixel rms ≤ 100 DN.
8. Acquired after camera reinstallation on 2018 February 5 UT.

When there were multiple fields, CCDs, and quadrants containing the source for a particular filter, we selected the reference image containing the largest number of high-quality ZTF science images in the co-add to be the reference image. We produced $1000'' \times 1000''$ cutouts of each single-epoch science image and reference image, produced subtractions, and then undertook aperture photometry with a $3''.0$ radius. We then applied the aperture to point-spread function (PSF) correction factors produced by the main ZTF image pipeline to produce PSF photometry light curves. We measured the baseline flux of each object in the reference image and added this to the fluxes measured from the image subtractions.

In order to improve our sensitivity to low signal-to-noise ratio variability from faintly varying AGN and prepare the data

for calculation of the Pearson correlation coefficient between g - and r -band photometry, we binned the data in temporal bins. We first applied zero-point corrections and then undertook error-weighted binning in flux space using bins of 5-, 10-, and 20-day increments. Therefore, each galaxy had three light curves with different bin sizes for the calculation of variability statistics. This binning procedure may have reduced our sensitivity to objects with optical variability only on timescales < 20 days and therefore may have introduced biases against particularly low-mass AGN. However, we determined that binning was necessary to allow for the calculation of the Pearson r correlation coefficient while confidently identifying light curves with correlated variability over a range of timescales, as expected from AGN power spectra (Kelly et al. 2009; MacLeod et al. 2011; Burke et al. 2021). With this procedure we generated light curves of 25,714 dwarf galaxies and the 1053 AGN from the high-mass galaxy control sample.

4. Selection of Variable IMBH Candidates

In order to detect real variability among the sample of dwarf galaxy light curves, we trialed a number of variability statistics, including the Pearson correlation coefficient (as used by Secret & Satyapal 2020), the goodness of fit of the light curves to the quasar structure function (using `qsffit` (Butler & Bloom 2011), as used in Baldassare et al. 2018, 2020b; Ward et al. 2021), the excess variance (Sánchez et al. 2017; Martínez-Palomera et al. 2020), and the χ^2/N in g and r bands. We found that a combination of the Pearson correlation coefficient and χ^2 produced the best separation between the AGN control sample and the majority of the nonvariable dwarf galaxy population.

The Pearson correlation coefficient r between the binned g - and r -band fluxes was calculated as

$$r = \frac{C_{f_g f_r}}{\sigma_{f_g} \sigma_{f_r}}, \quad (1)$$

where $C_{f_g f_r}$ is the covariance between g and r bands given by

$$C_{f_g f_r} = \frac{1}{N-1} \sum_i (f_{g,i} - \langle f_g \rangle) \times (f_{r,i} - \langle f_r \rangle), \quad (2)$$

σ_{f_g} and σ_{f_r} are the g - and r -band variability amplitudes given by

$$\sigma_f^2 = \frac{1}{N-1} \sum_i (f_i - \langle f \rangle)^2, \quad (3)$$

and the expectation value $\langle f \rangle$ was given by the median flux.

We also calculated the χ^2/N of the light curves in g and r bands:

$$\chi^2/N = \frac{1}{N} \sum_i \frac{(f_i - \langle f \rangle)^2}{\sigma_i^2}. \quad (4)$$

The distribution of the Pearson correlation coefficient r and the χ^2/N values for g and r bands for the dwarf galaxy and control AGN light curves with 5-, 10-, and 20-day bin sizes is shown in Figure 1. We applied cutoffs of $r > 0.2$, $r > 0.3$, and $r > 0.4$ for 5-, 10-, and 20-day bin sizes, respectively, and $\chi^2/N > 3$ in both filters for all bin sizes, to classify dwarf galaxies as variable. Each dwarf galaxy was required to meet this cutoff in all three binning timescales to ensure that correlations and variance were not produced as artifacts of bin phase and size.

¹¹ <https://github.com/zuds-survey/zuds-pipeline>

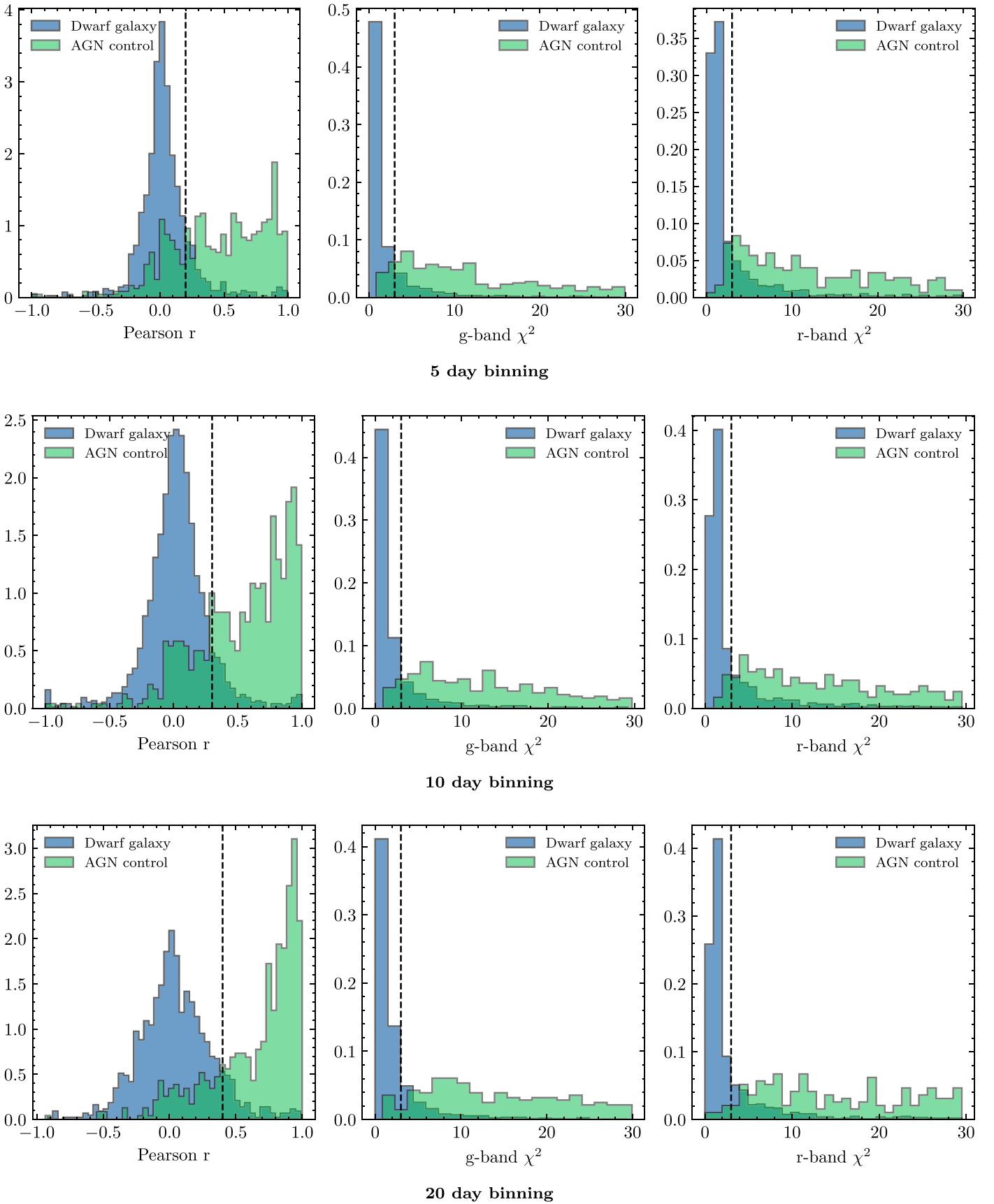


Figure 1. Pearson r correlation coefficient and χ^2/N in g and r band calculated from ZTF light curves for three different binning timescales. We show the entire dwarf galaxy population with ZTF photometry in blue and the AGN control sample (from host galaxies of stellar mass $M_* > 3 \times 10^{9.75} M_\odot$) in green. The cutoffs used for AGN candidate selection are shown with black dotted lines for each statistic. We required the three statistics to satisfy the cutoffs for all three binning timescales in order for a candidate to be selected.

Table 1
Properties of the ZTF-selected IMBH Candidates

NSA ID	R.A. (hms)	Decl. (dms)	z	$\log_{10} M_* (M_\odot)$	$\log_{10} M_{\text{BH}} (M_\odot)$	BPT Class	BLR?	Virial $\log_{10} M_{\text{BH}} (M_\odot)$
8479	12:31:07.418	00:27:47.447	0.0214	9.51	6.95	SF	×	...
19864	12:36:43.723	-3:01:15.176	0.0082	8.12	5.23	SF	×	...
20245	12:42:32.662	-1:21:02.583	0.0037	8.75	6.01	SF	×	...
23518	16:21:41.608	01:02:53.989	0.0324	9.57	7.03	SF	×	...
30890	23:18:28.463	00:20:47.845	0.0341	9.66	7.14	Composite	×	...
32653	00:09:26.408	00:19:32.182	0.1138	9.74	7.24	Seyfert	✓	7.048
35747	01:10:59.314	00:26:01.103	0.0188	9.7	7.19	Seyfert	✓	7.561
37197	01:44:32.794	00:57:15.492	0.0716	9.59	7.05	SF	×	...
42027	00:43:38.702	14:38:29.188	0.0766	9.74	7.24	SF	×	...
43101	01:06:29.847	14:58:17.054	0.0393	9.54	6.99	SF	×	...
44934	02:11:58.218	14:16:09.393	0.0264	9.45	6.88	SF	×	...
46229	07:47:06.104	37:36:55.296	0.0364	9.54	6.99	SF	×	...
49405	08:29:12.677	50:06:05.241	0.0432	9.54	6.99	SF	✓	6.363
52237	09:16:08.642	55:59:22.952	0.0721	9.67	7.15	SF	×	...
78310	09:05:10.183	50:42:10.045	0.0369	9.74	7.24	SF	×	...
83637	10:19:48.118	03:31:18.466	0.0324	9.05	6.38	SF	×	...
95377	15:23:50.527	56:48:15.474	0.0511	9.41	6.83	SF	×	...
97216	16:05:40.674	50:45:16.842	0.0129	8.2	5.33	SF	×	...
115553	02:54:57.457	00:25:55.471	0.1077	9.47	6.9	SF	×	...
117445	22:16:19.958	-7:20:55.229	0.0591	9.15	6.51	SF	×	...
127775	00:17:18.375	15:49:06.185	0.0603	9.36	6.77	SF	×	...
132743	09:49:53.016	60:53:25.584	0.0828	9.57	7.03	SF	×	...
133634	11:00:44.374	60:20:05.121	0.0171	8.46	5.65	SF	×	...
138748	14:55:45.198	57:20:49.518	0.0795	9.56	7.01	SF	×	...
142229	15:57:46.352	47:17:47.018	0.0316	9.35	6.75	SF	×	...
142571	16:20:58.965	45:10:54.736	0.0542	9.51	6.95	Composite	×	...
158589	11:30:27.424	52:18:13.171	0.0483	9.37	6.78	SF	×	...
159003	11:41:52.296	52:38:24.914	0.0191	8.91	6.21	SF	×	...
164884	09:28:01.292	49:18:17.303	0.1143	9.71	7.2	SF	✓	6.961
168943	13:45:010.34	-3:01:20.764	0.0469	9.42	6.84	SF	×	...
181600	13:06:15.181	58:57:0033.1	0.0292	9.64	7.11	Seyfert	✓	6.732
183841	11:09:18.046	49:47:53.629	0.0466	9.3	6.69	SF	×	...
188282	17:15:34.141	31:31:45.348	0.0229	9.61	7.08	SF	×	...
189758	21:05:04.972	00:01:010.03	0.0312	9.46	6.89	Composite	×	...
197553	10:57:14.371	54:10:56.999	0.072	9.34	6.74	SF	×	...
198091	11:32:00.219	53:42:50.763	0.0268	9.62	7.09	SF	×	...
202748	21:24:056.67	00:38:45.601	0.048	9.19	6.56	SF	×	...
212423	16:18:03.954	35:08:08.626	0.033	9.59	7.05	SF	×	...
272369	11:38:55.181	44:19:031.64	0.0321	9.45	6.88	Composite	×	...
277358	14:52:32.685	36:24:47.857	0.0542	9.52	6.96	SF	×	...
298494	12:19:51.136	47:50:37.875	0.0384	9.71	7.2	Seyfert	×	...
301868	13:25:45.394	46:07:01.166	0.0365	9.25	6.63	SF	×	...
451469	14:14:05.019	26:33:36.804	0.0358	9.66	7.14	SF	✓	6.303
545880	13:37:02.948	18:10:13.979	0.0265	8.82	6.1	SF	×	...

Note. Properties of the 44 AGN candidates with significant and correlated g - and r -band variability found in ZTF. The IDs, positions, redshifts, and host galaxy stellar masses are those from the NSA catalog version $v_{1.0.1}$. In the first $\log_{10} M_{\text{BH}}$ column we show the estimated BH mass based on the $M_* - M_{\text{BH}}$ relation from Schutte et al. (2019), which has a scatter of 0.68 dex. The presence of Balmer broad lines is indicated in the BLR column. Virial masses were calculated for broad-line AGN by Ho & Kim (2015) based on the width of the H α broad lines.

After applying these cutoffs, we found 130 dwarf galaxies with statistically significant variability.

We then manually inspected the light curves and difference images to remove light curves with high variance due to poor-quality photometry and to determine which light curves contained single flares with reddening consistent with SNe. A total of 36 SN-like flares were found, corresponding to a nuclear SN rate of $0.14\% \pm 0.02\%$ ($0.05\% \pm 0.01\% \text{ yr}^{-1}$) for dwarf galaxies in ZTF Phase I.

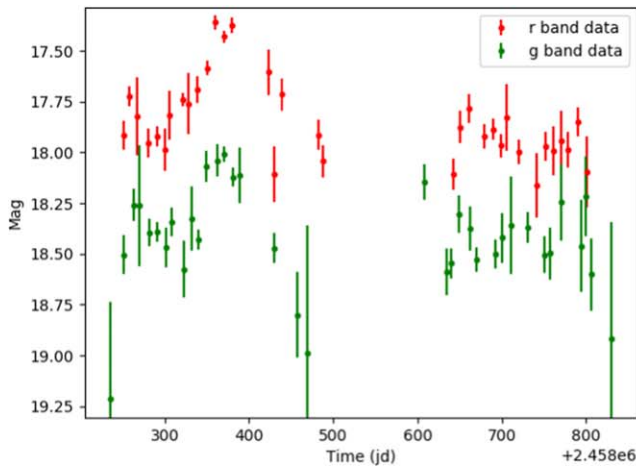
This process produced a final sample of 44 dwarf galaxies ($0.17\% \pm 0.03\%$) with variability consistent with AGN activity. These constitute our set of optically variable IMBH candidates. The properties of this sample are summarized in

Table 1. Examples of ZTF light curves of three dwarf galaxies with AGN-like variability are shown in Figure 2, and examples of three SN light curves are shown in Figure 3.

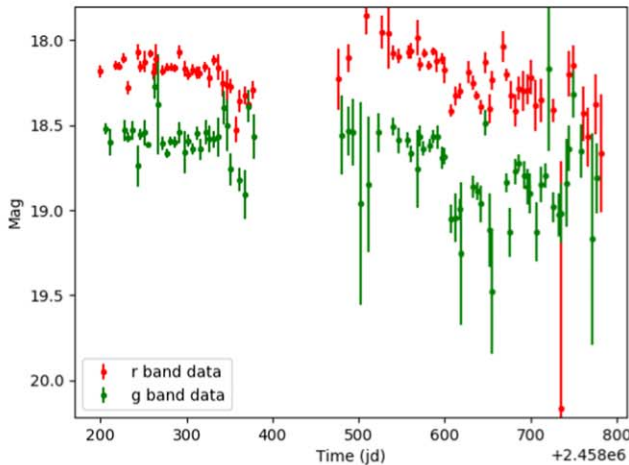
The distributions of the redshifts and host galaxy stellar masses of the optically variable dwarf galaxies are shown in Figure 4. All but six of the IMBH candidates were in galaxies of mass $M_* > 10^9 M_\odot$. By comparison, a larger fraction of SNe were observed in low-mass galaxies, and most were found in a narrow redshift range of $0.02 < z < 0.055$.

We checked both the SN and AGN candidate samples for spectroscopic classification on the Transient Name Server.¹² A

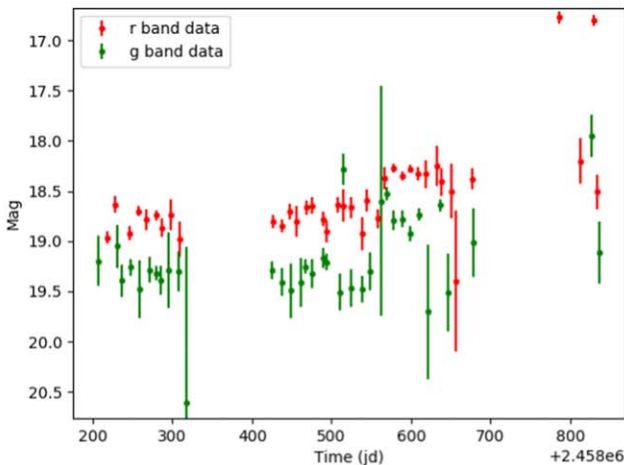
¹² <https://www.wis-tns.org/>



NSA189758



NSA212423



NSA158589

Figure 2. Three examples of ZTF light curves that passed the variability criteria and were classified as variable AGN candidates.

total of 25 of the 36 SN candidates had published spectroscopic classifications. One of these was classified as an SN but was not typed. A total of 17 out of the remaining 24 (71%) were

classified as SN Ia, SN Ic, or SN Ic-BL. A total of 7 out of 24 (29%) were classified as SN II or SN IIn. These classifications are shown in Table 2. We note that the remaining 11 SNe without spectroscopic classifications can only be classified as SN candidates, as they may be AGN outbursts (Drake et al. 2019). None of the AGN candidates had spectroscopic classifications published on TNS.

In order to estimate the BH masses of our IMBH candidates based on their host galaxy stellar mass, we used the updated relationship between BH mass and bulge mass derived by Schutte et al. (2019). This study found a linear relationship based on a sample of galaxies with carefully measured BH and bulge masses, including eight dwarf galaxies with stellar masses $\log(M_*) < 8.5 M_\odot$:

$$\begin{aligned} \log(M_{\text{BH}}/M_\odot) &= \alpha + \beta \log(M_*/10^{11}M_\odot) \\ \alpha &= 8.80 \pm 0.085; \beta = 1.24 \pm 0.081. \end{aligned} \quad (5)$$

The relation has a scatter of 0.68 dex. The BH mass estimates for the IMBH candidates are shown in Table 1.

5. Spectroscopic and Multiwavelength Properties of the ZTF-selected IMBH Candidates

In order to determine the spectroscopic class of the IMBH candidates on the Baldwin, Phillips, and Terlevich diagram (Baldwin et al. 1981; Veilleux & Osterbrock 1987), we fit the narrow emission line ratios with penalized pixel fitting (pPXF; Cappellari & Emsellem 2004; Cappellari 2016). This method finds the best-fit stellar continuum and absorption model using a large sample of high-resolution templates of single stellar populations adjusted to match the spectral resolution of the input spectrum. We simultaneously fit the narrow $\text{H}\alpha$, $\text{H}\beta$, $\text{H}\gamma$, $\text{H}\delta$, $[\text{S II}] \lambda\lambda 6717, 6731$, $[\text{N II}] \lambda\lambda 6550, 6575$, $[\text{O I}] \lambda\lambda 6302, 6366$ and $[\text{O III}] \lambda\lambda 5007, 4959$ emission lines and the best-fit stellar continuum spectrum during template fitting.

The classification of the IMBH candidates on the $[\text{O III}] \lambda 5007/\text{H}\beta - [\text{N II}] \lambda 6583/\text{H}\alpha$ BPT diagram is shown in Figure 5. A total of 35 objects (81%) are classified as star-forming, while four objects (9%) are in the composite region and four (9%) are classified as Seyferts. For comparison, we also show the density of the original 81,462 dwarf galaxy parent sample on the BPT diagram using emission-line ratios quoted in the NSA catalog. From the gray contours it can be seen that the majority of the dwarf galaxy population is star-forming but a small population extends out to AGN and LINER regions of the BPT classification scheme. Our typical star-forming IMBH candidates lie at higher emission-line ratios than this population, in part because our pPXF modeling considers stellar absorption of those lines.

The classification of the SN host galaxies on the $[\text{O III}] \lambda 5007/\text{H}\beta - [\text{N II}] \lambda 6583/\text{H}\alpha$ BPT diagram is also shown in Figure 5. A total of 34 host galaxies (94%) are classified as star-forming, while one object (3%) was in the composite region and one (3%) was in the Seyfert region.

We cross-matched our ZTF-selected IMBH candidates to the active dwarf galaxies from the Secrest & Satyapal (2020) mid-IR variability search, the Baldassare et al. (2018, 2020b) optical variability searches, the Molina et al. (2021) $[\text{Fe X}] \lambda 6374$ coronal line emission search, the Mezcua & Domínguez Sánchez (2020) IFU spectroscopy search, the Mezcua et al. (2018) Chandra X-ray search, the Latimer et al. (2021) mid-IR color selection box search, and the Reines et al. (2013) optical emission-line search. We found that only seven objects had

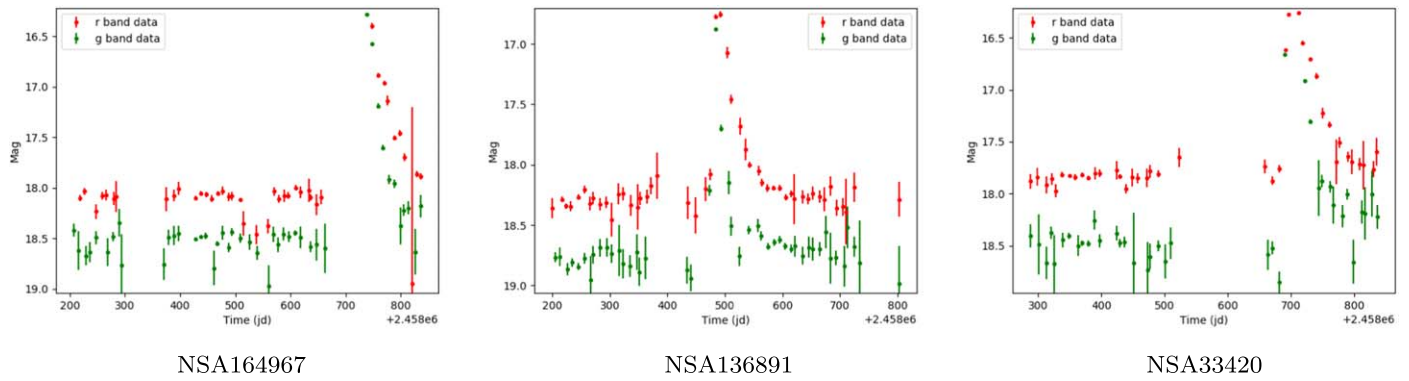


Figure 3. Three examples of ZTF light curves that passed the variability criteria and were classified as SN candidates.

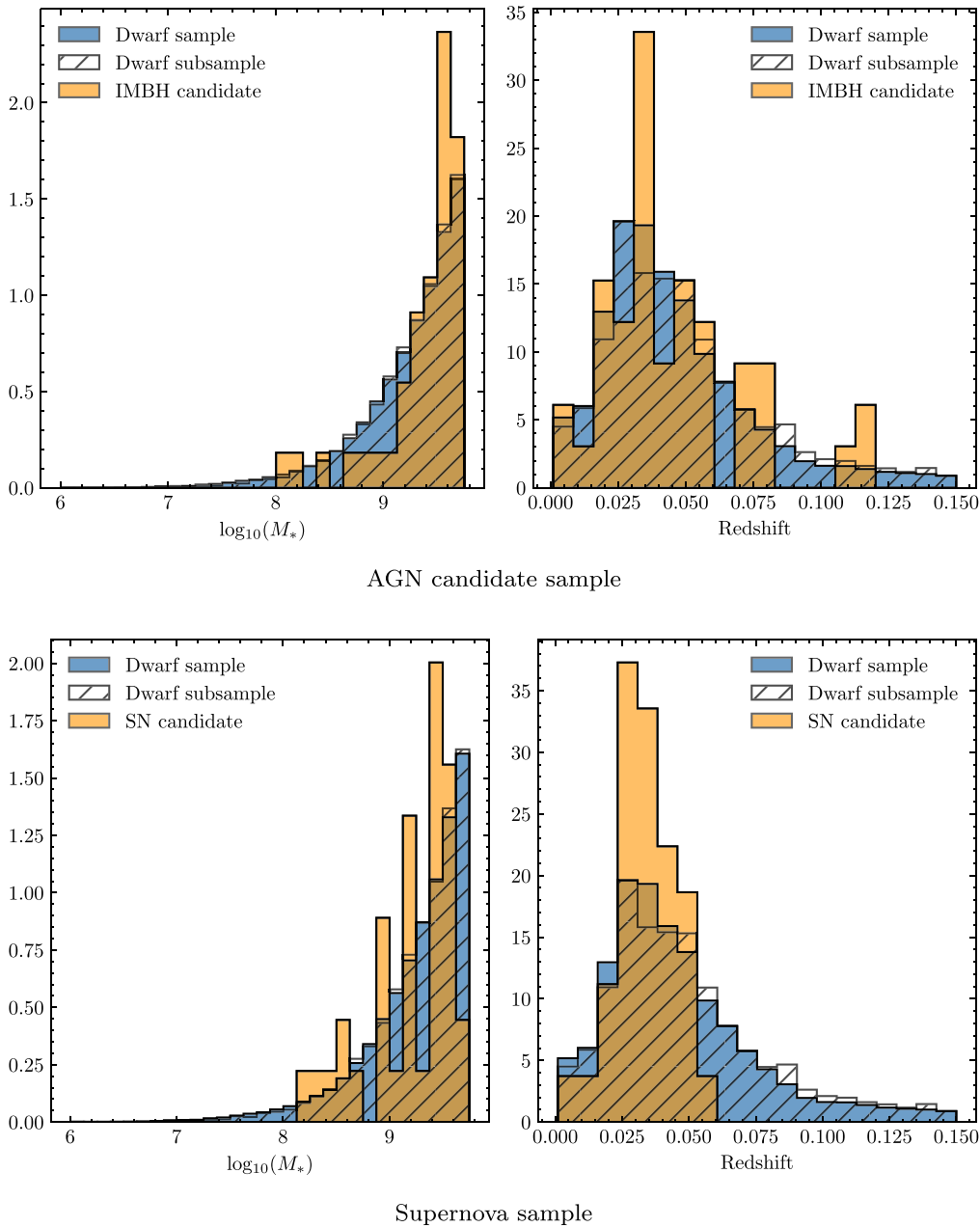


Figure 4. Normalized galaxy mass and redshift distributions of variable IMBH candidates (top) and SN candidates (bottom) shown in green and the parent dwarf galaxy sample shown in blue. The subset of the parent dwarf galaxy for which ZTF photometry was produced for the optical IMBH search is shown in the hatched histogram. Redshifts and host galaxy mass measurements were derived from the NSA.

Table 2
Properties of the ZTF-selected Supernovae in Dwarf Galaxies

NSA ID	R.A. (hms)	Decl. (dms)	z	$\log_{10}M_*$ (M_\odot)	BPT Class	BLR?	Classification
6971	12:00:49.206	-1:15:01.297	0.021	8.55	SF	×	None
8600	12:35:43.642	00:13:25.722	0.0231	9.43	Seyfert	×	None
14878	14:48:27.429	00:12:04.871	0.0269	8.94	SF	×	None
33420	00:28:51.572	-1:04:22.318	0.0333	9.25	SF	×	SN Ia
38750	02:33:46.936	-1:01:28.378	0.0489	9.51	SF	×	None
41092	03:35:26.631	00:38:11.445	0.0232	8.23	SF	×	None
47343	08:00:26.505	42:49:16.255	0.0408	9.58	SF	×	SN Ia
60574	10:26:03.501	64:50:10.285	0.0368	9.47	SF	×	SN Ia
60660	10:40:58.604	65:30:54.366	0.0108	8.25	SF	×	SN Ic
70478	13:02:24.185	03:22:032.91	0.0234	9.25	SF	×	None
77819	08:35:16.365	48:19:01.178	0.0429	9.55	SF	×	SN Ic
81368	08:55:49.031	03:38:32.333	0.0274	9.59	SF	×	SN IIn
90779	11:11:03.618	64:14:46.086	0.0352	9.46	SF	×	SN II
121437	21:51:07.575	12:25:36.661	0.0285	9.46	SF	×	SN Ic-BL
126810	23:58:48.168	14:44:29.893	0.0274	8.95	SF	×	SN II
136564	13:21:28.156	62:52:029.91	0.0413	9.66	SF	×	SN Ia
136891	13:29:31.023	61:26:000.53	0.0313	9.25	SF	×	None
137293	14:02:21.316	59:25:08.501	0.0321	9.61	SF	×	None
137916	14:17:15.746	59:16:39.876	0.0365	9.24	SF	×	SN Ia
141203	03:26:45.983	01:11:01.017	0.0485	9.13	SF	×	SN Ia
146295	11:19:04.838	03:42:53.379	0.0273	8.74	SF	×	None
164967	09:35:11.377	48:43:08.652	0.0244	8.9	SF	×	SN Ia
183178	10:43:31.995	48:26:37.354	0.0413	9.44	SF	×	SN Ia
191873	09:36:08.603	06:15:25.511	0.008	8.43	SF	×	SN
208509	14:20:52.371	50:31:28.532	0.0446	9.52	SF	×	SN II
211965	16:12:50.281	36:01:18.328	0.0314	9.09	SF	×	None
214163	02:36:15.641	-1:11:59.948	0.0471	9.2	SF	×	SN Ia
216212	00:13:45.056	00:51:05.651	0.0322	8.55	SF	×	None
220206	14:49:48.132	54:48:46.962	0.0448	9.47	SF	×	SN Ia
224290	16:57:15.706	31:57:50.583	0.0377	9.3	SF	×	SN II
229236	09:04:08.208	39:40:35.155	0.028	9.5	SF	×	SN Ia
249950	15:08:50.831	40:42:44.478	0.0305	9.38	SF	×	SN II
269844	10:23:20.137	41:23:40.255	0.0515	9.6	SF	×	SN Ia
271156	11:02:16.807	44:20:06.661	0.0246	9.64	Composite	×	SN II
289679	10:15:29.897	37:59:02.588	0.054	8.93	SF	×	SN Ia
298529	12:22:36.827	47:58:08.744	0.0499	9.5	SF	×	SN Ia

Note. Properties of the 36 SN candidates with significant and correlated g - and r -band variability found in ZTF. The IDs, positions, redshifts, and host galaxy stellar masses are those from the NSA catalog version $v_{1.0.1}$. The presence of Balmer broad lines is indicated in the BLR column. The last column shows the spectroscopic classification published by ZTF on the Transient Name Server.

been detected in previous optical variability searches (Baldassare et al. 2018, 2020b), where they have different IDs owing to the use of NSA version $v_{0.1.2}$: NSA32653 (SDSS), NSA49405 (PTF), NSA115553 (SDSS), NSA181600 (PTF), NSA202748 (PTF), NSA451469 (PTF), and NSA545880 (PTF). No other multiwavelength detections of our candidates from previous IMBH searches were found.

NSA32653, NSA35747, NSA49405, NSA164884, NSA464884, NSA181600, and NSA451469 were the only objects in our IMBH sample to exhibit broad Balmer lines in archival SDSS spectra. These objects previously had their virial BH masses estimated using the width of the $H\alpha$ broad lines by Ho & Kim (2015) and Liu et al. (2019). These virial masses ranged between $10^{6.3}$ and $10^{7.6} M_\odot$ and are shown in Table 1.

6. ZTF Variability of Previously Reported PTF-selected IMBH Candidates

After discovering that five objects from the variability-selected AGN sample from PTF (Baldassare et al. 2020b) were

also variable in ZTF according to our selection thresholds, we decided to determine whether the remaining AGN candidates in dwarf galaxies from PTF had ZTF variability that was missed by our selection criteria.

We first found that our parent dwarf galaxy sample had 152 objects that overlapped with the variable PTF sample. We then visually inspected the `zuds-pipeline` light curves we made of the 152 common dwarf galaxies and confirmed that no other dwarf galaxy had apparent variability. We then used the ZTF forced photometry service (Masci et al. 2019) to obtain alternative photometry of the sources with the original ZTF reference images. After removing poor-quality images by requiring that the `procstatus` flag be $= 0$, we measured the baseline flux from the reference images, applied zero-points, and combined the baseline and single-epoch fluxes to produce the light curves of the 152 objects. We then visually inspected the candidates to look for any signs of variability. The alternative pipeline confirmed that only five candidates from our overlapping samples showed statistically significant variability in ZTF.

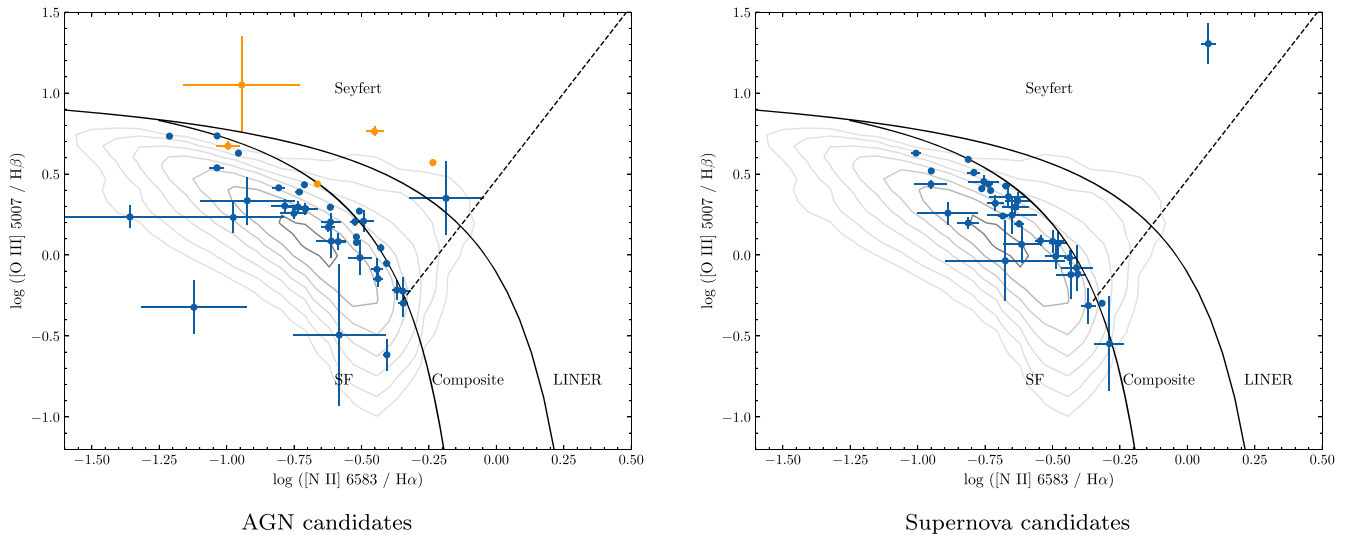


Figure 5. BPT diagram showing narrow line ratios derived from p PXF fitting of archival SDSS spectra of the ZTF-selected IMBH candidates (left) and SN candidates (right). Orange points show line ratios for IMBH candidates with broad Balmer lines in archival spectra, and blue points show those with narrow emission lines only. Gray contours show the population density with log scaling of the entire parent dwarf galaxy sample for line ratios derived from the NASA-Sloan Atlas. Classification regions are labeled in black text. We note that because p PXF determines narrow emission line strength after accounting for stellar absorption of those same lines, fluxes may appear to be slightly larger in the BPT diagram compared to the NSA-derived emission-lines fluxes of the dwarf galaxy population.

7. WISE Single-epoch Forced Photometry

As we aimed to search for mid-IR variability from a large sample of dwarf galaxies that may have been too faint to appear in the search of the original AllWISE catalog by Secrest & Satyapal (2020), we made use of forward-modeled photometry of time-resolved WISE co-adds (Meisner et al. 2018) made available through Data Release 9¹³ of the DESI imaging Legacy Survey (Dey et al. 2019). This approach was previously implemented by Lang et al. (2016b) to produce forced photometry of 400 million SDSS sources with the deep unWISE co-adds (Lang 2014; Meisner et al. 2017). Lang et al. (2016b) used *The Tractor* (Lang et al. 2016a) to use deeper, higher-resolution source models from SDSS to produce photometry of blended and faint objects in the unWISE co-adds. They were able to report fluxes and uncertainties from 3σ and 4σ detections that were not included in the original WISE catalog. More recently, they implemented this technique to produce time-resolved WISE photometry (Meisner et al. 2018). As WISE revisits each field at a ~ 6 -month cadence, with an increased cadence toward the poles, and takes ~ 10 exposures each visit, they co-added the exposures from each visit to produce forced photometry on each co-add. This therefore provided light curves with approximately 15 fluxes measured over ~ 8 yr.

We cross-matched the SDSS galaxy positions of our dwarf galaxy sample to the unWISE source catalog and pulled the single-epoch WISE photometry for the closest unWISE source. Some light curves showed an oscillation behavior when multiple sources were contained within the large WISE PSF and the WISE flux was distributed across the multiple sources differently in each epoch. To overcome this, we combined the total flux of the sources within a radius of 3 WISE pixels ($3'' \times 2''.75$) to ensure that all dwarf galaxy variability was captured within the combined fluxes. We removed light curves where an erroneously high flux ($f - \langle f \rangle > 5\sigma$) in both W1 and W2 bands produced an r and χ^2/N above the cutoffs. We also

removed light curves where source confusion within the WISE PSF size still resulted in an oscillating behavior using the following criteria. If the summed difference between every adjacent W1 flux measurement was greater than twice the summed difference between every W1 flux offset by two epochs, the light curve was flagged as bad quality. We produced WISE light curves of the AGN control sample with the same procedure.

For each source we calculated the Pearson correlation coefficient r between the W1 and W2 bands and the χ^2/N for each band. The distribution of these statistics for the two samples is shown in Figure 6. We required that dwarf galaxies have $r > 0.75$ and $\chi^2/N > 1.0$ in W1 and W2 to be considered a variable AGN candidate.

Of the 79,879 dwarf galaxies for which WISE single-epoch forced photometry was available, 124 were removed owing to light-curve quality flags. Of the remaining 79,755 light curves, we found that 165 had fluxes that met our variability criteria. One dwarf galaxy, NSA253466, was detected by our variability criteria owing to the well-studied Type IIIn SN 2010jl (Stoll et al. 2011), which has had detailed follow-up in the near-IR, X-ray, and radio (e.g., Fransson et al. 2014; Chandra et al. 2015) showing interaction with the dense circumstellar medium. We removed this object from our AGN candidate sample. We removed three other objects with SNe visible in both WISE and ZTF data: NSA559938 (ZTF18aamftst, an SN IIIn), NSA143427 (ZTF18acwyvet, an SN IIL), and NSA230430 (ZTF20aaukpac, an SN Ia). We removed 14 other galaxies with light curves showing single flares, often with color changes characteristic of SNe: NSA20892, NSA32356, NSA143207, NSA236644, NSA250558, NSA253466, NSA274965, NSA340533, NSA355173, NSA379733, NSA475418, NSA502699, NSA528212, and NSA548379. The properties of these SN host galaxies are summarized in Table 3.

The properties of the remaining final sample of 148 AGN candidates (corresponding to $0.19\% \pm 0.02\%$ of the dwarf galaxy sample) are summarized in Table 4, and six examples of variable WISE light curves are shown in Figure 7.

¹³ <https://www.legacysurvey.org/dr9/catalogs/>

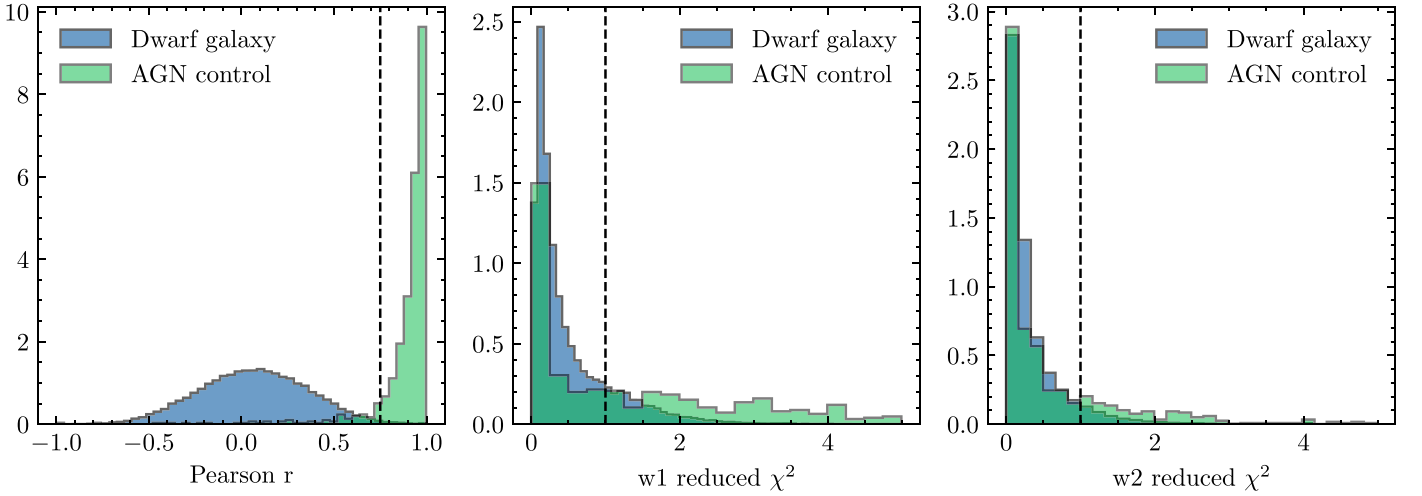


Figure 6. Pearson r correlation coefficient and χ^2/N in W1 and W2 band calculated from WISE forward-modeling light curves. We show the entire dwarf galaxy population with WISE photometry in blue and the AGN control sample (from host galaxies of stellar mass $M_* > 3 \times 10^{9.75} M_\odot$) in green. The cutoffs used for AGN candidate selection are shown with black dotted lines for each statistic. We required the three statistics to satisfy the cutoffs in order for a candidate to be selected.

Table 3
Properties of the 14 SN Candidates from WISE

NSA ID	R.A. (hms)	Decl. (dms)	z	$\log_{10} M_* (M_\odot)$	$\log_{10} M_{\text{BH}} (M_\odot)$	BPT Class	BLR?	SN Class
20892	12:59:05.105	-03:12:14.257	0.0101	8.19	5.31 ± 0.68	SF	×	None
32356	00:10:05.515	-01:05:39.795	0.0379	9.43	6.85 ± 0.68	SF	×	None
143207	16:28:31.291	41:37:12.833	0.0331	9.59	7.05 ± 0.68	SF	×	None
143427	16:32:03.899	39:36:31.289	0.0281	9.27	6.66 ± 0.68	SF	×	SN IIL
230430	07:51:08.935	22:44:27.419	0.0288	9.25	6.63 ± 0.68	...	×	SN Ia
236644	11:43:039.35	09:50:18.863	0.0202	8.77	6.03 ± 0.68	SF	×	None
250558	15:31:51.855	37:24:047.41	0.0299	9.26	6.65 ± 0.68	...	×	None
253466	09:42:53.245	09:29:36.066	0.0106	9.06	6.4 ± 0.68	...	×	None
274965	13:08:19.122	43:45:25.483	0.0365	9.57	7.03 ± 0.68	...	×	None
355173	15:28:40.931	10:33:28.095	0.0887	9.71	7.19 ± 0.68	SF	✓	None
379733	13:32:18.328	07:56:26.052	0.0236	9.57	7.03 ± 0.68	SF	×	None
502699	10:08:07.779	19:17:57.808	0.0335	9.5	6.94 ± 0.68	Composite	×	None
548379	13:20:53.681	21:55:10.518	0.0224	8.63	5.86 ± 0.68	...	×	None
559938	14:31:14.719	17:11:35.152	0.0378	9.38	6.79 ± 0.68	SF	×	SN IIn

Note. Properties of the 14 SN candidates found in forward-modeled WISE light curves. The IDs, positions, redshifts, and host galaxy stellar masses are those from the NSA catalog version $v_{1.0.1}$. In the $\log_{10} M_{\text{BH}}$ column we show the estimated BH mass based on the $M_* - M_{\text{BH}}$ relation from Schutte et al. (2019), which has a scatter of 0.68 dex. The presence of Balmer broad lines is indicated in the BLR column. The last column shows the spectroscopic classification published by ZTF on the Transient Name Server.

8. Properties of the WISE-selected Variable IMBH Candidates

The distributions of the redshifts and host stellar masses of the mid-IR variable dwarf galaxies are shown in Figure 8. We exclude NSA64525 from the histogram because the estimated mass provided by the NASA-Sloan Atlas ($10^{5.39} M_\odot$) is inconsistent with the stellar dispersion velocity of $193 \pm 8 \text{ km s}^{-1}$ measured by the SDSS spectroscopic pipeline. This dispersion velocity indicates that the BH itself likely has a mass of $\sim 10^7 M_\odot$ according to the $M - \sigma_*$ relation (Kormendy & Ho 2013), and the host galaxy therefore has mass comparable to $\sim 10^{9.5} M_\odot$ based on the $M_{\text{BH}} - M_*$ relation (Schutte et al. 2019). The mid-IR variability selection finds a higher fraction of variable AGN at low redshifts compared to the overall dwarf galaxy sample and shows a slight preference for higher-mass galaxies.

The classification of the mid-IR IMBH candidates on the [O III] $\lambda 5007/\text{H}\beta - [\text{N II}] \lambda 6583/\text{H}\alpha$ BPT diagram is shown in

Figure 9. A total of 100 objects (69%) are classified as star-forming, while 32 objects (22%) are in the composite region, 3 (2.1%) were classified as LINERs, and 10 (6.9%) were classified as Seyferts. A total of 12 of the IMBH candidates (8.1%) have broad Balmer lines. These objects also had their virial BH masses estimated using the width of the $\text{H}\alpha$ broad lines by Ho & Kim (2015) and Liu et al. (2019). These virial masses range between $10^{5.5}$ and $10^{8.2} M_\odot$, respectively, and are shown in Table 4.

In order to determine how many WISE-selected IMBH candidates were also optically variable, we produced ZTF photometry of the remainder of the 148 dwarf host galaxies that were not included in the original ZTF search. We found that 15 out of 148 (10%) met the optical variability criteria for ZTF outlined in Section 4. Seven of the 15 AGN that were variable at both wavelengths had visible broad lines in their spectra, and among these broad-line AGN, the virial masses ranged between $M_{\text{BH}} = 10^{6.3} M_\odot$ and $M_{\text{BH}} = 10^{8.2} M_\odot$. Only two of these

Table 4
Properties of the 148 WISE-selected IMBH candidates

NSA ID	R.A. (hms)	Decl. (dms)	z	$\log_{10}M_*$ (M_{\odot})	$\log_{10}M_{\text{BH}}$ (M_{\odot})	BPT Class	BLR?	$\log_{10}M_{\text{BH,vir}}$ (M_{\odot})	Optical Var.?
3045	10:39:44.299	00:51:28.625	0.0253	8.88	6.17 ± 0.68	SF	×	...	×
12740	14:06:30.104	00:19:39.525	0.1063	8.93	6.24 ± 0.68	SF	✓	6.436	×
34102	00:45:000.51	00:47:23.578	0.0568	9.63	7.1 ± 0.68	SF	×	...	×
47457	08:03:38.042	43:20:034.99	0.0153	9.35	6.75 ± 0.68	SF	×	...	×
50093	08:38:19.706	51:31:52.998	0.0166	9.03	6.35 ± 0.68	SF	×	...	×
50870	08:48:04.539	52:14:09.051	0.0403	9.6	7.07 ± 0.68	Seyfert	×	...	×
54469	03:19:26.057	-6:07:015.98	0.0076	9.45	6.87 ± 0.68	SF	×	...	×
64525	10:11:03.771	02:31:45.452	0.1211	5.39	1.84 ± 0.68	LINER	×	...	×
71121	13:19:40.797	03:24:33.828	0.0218	8.27	5.42 ± 0.68	SF	×	...	×
73327	14:10:052.96	01:22:10.396	0.026	9.73	7.23 ± 0.68	SF	×	...	×
74770	14:58:54.268	01:59:027.33	0.0298	9.49	6.93 ± 0.68	SF	×	...	×
75025	15:05:07.305	01:59:51.121	0.008	8.73	5.99 ± 0.68	...	×	...	×
81096	08:41:34.335	02:11:19.877	0.0287	8.93	6.23 ± 0.68	SF	×	...	×
87109	14:19:27.498	04:45:13.802	0.1434	9.66	7.13 ± 0.68	LINER	×	...	✓
93256	14:02:059.68	61:45:03.942	0.0054	9.33	6.73 ± 0.68	Composite	×	...	×
95784	15:40:37.104	58:15:035.93	0.0501	9.64	7.11 ± 0.68	SF	×	...	×
98016	16:06:33.607	48:39:37.056	0.0437	9.48	6.91 ± 0.68	Composite	×	...	×
102352	20:58:22.143	-6:50:04.353	0.0738	9.72	7.21 ± 0.68	Seyfert	✓	6.432	✓
106103	00:01:11.154	-10:01:55.702	0.0489	9.65	7.12 ± 0.68	Seyfert	✓	6.372	×
107142	00:23:55.671	-9:24:22.513	0.0522	9.57	7.03 ± 0.68	Composite	×	...	×
111190	01:52:32.835	-8:25:058.66	0.0176	9.45	6.88 ± 0.68	SF	×	...	×
112816	23:09:22.927	01:00:002.16	0.0153	9.14	6.49 ± 0.68	SF	×	...	×
120721	21:30:046.71	11:12:54.805	0.0475	9.62	7.09 ± 0.68	SF	×	...	×
124852	23:26:18.717	14:11:50.593	0.0417	9.49	6.93 ± 0.68	Composite	×	...	×
128577	07:47:55.395	34:02:12.144	0.0159	9.1	6.45 ± 0.68	SF	×	...	×
129617	08:12:26.587	39:32:19.995	0.0326	9.74	7.24 ± 0.68	SF	×	...	×
130265	08:32:24.255	43:06:07.807	0.0247	9.12	6.47 ± 0.68	SF	×	...	×
135650	12:40:057.29	63:31:010.47	0.0083	9.67	7.14 ± 0.68	Composite	×	...	×
143517	16:31:24.055	41:22:44.657	0.0309	9.47	6.91 ± 0.68	SF	×	...	×
152094	13:16:059.37	03:53:19.809	0.0454	9.71	7.2 ± 0.68	Seyfert	×	...	×
155198	08:17:15.852	31:39:07.139	0.0452	9.72	7.21 ± 0.68	Composite	×	...	×
164884	09:28:01.292	49:18:17.303	0.1143	9.71	7.21 ± 0.68	SF	✓	6.961	×
175367	09:09:33.556	38:42:38.594	0.0561	9.69	7.17 ± 0.68	SF	×	...	×
178387	10:39:28.739	56:20:58.148	0.0748	9.61	7.08 ± 0.68	Seyfert	✓	6.515	✓
180304	12:03:38.324	58:59:11.804	0.0469	9.6	7.06 ± 0.68	SF	×	...	×
185495	12:05:21.947	50:14:11.506	0.0341	8.8	6.08 ± 0.68	SF	×	...	×
186717	17:02:01.824	31:53:01.341	0.0332	9.54	6.99 ± 0.68	SF	×	...	×
189025	20:46:38.107	00:20:21.688	0.0126	9.73	7.22 ± 0.68	LINER	×	...	×
208212	14:07:02.979	50:43:14.611	0.0072	8.34	5.51 ± 0.68	Composite	×	...	×
215346	01:15:37.856	00:12:58.114	0.0453	9.49	6.93 ± 0.68	SF	×	...	×
234033	09:54:38.791	40:32:04.395	0.0673	9.52	6.97 ± 0.68	Seyfert	✓	6.657	×
235055	11:01:16.027	10:16:17.924	0.0358	9.47	6.9 ± 0.68	SF	×	...	×
239541	12:33:07.855	10:14:56.145	0.0531	9.61	7.08 ± 0.68	SF	×	...	×
241996	10:29:28.222	09:50:01.145	0.0224	9.13	6.48 ± 0.68	SF	×	...	×
249598	14:26:31.705	44:51:42.018	0.0079	9.04	6.36 ± 0.68	SF	×	...	×
250824	08:07:00.613	05:37:37.137	0.052	9.47	6.9 ± 0.68	SF	×	...	×
266623	14:15:45.723	40:06:19.138	0.0202	9.73	7.22 ± 0.68	SF	×	...	×
267136	14:42:17.705	40:02:006.81	0.0266	8.87	6.16 ± 0.68	SF	×	...	×
273124	11:59:05.594	45:49:13.767	0.024	9.56	7.01 ± 0.68	Composite	×	...	×
278949	15:36:19.446	30:40:056.33	0.0059	8.36	5.52 ± 0.68	SF	×	...	×
280953	16:11:14.252	25:11:56.413	0.0475	9.61	7.08 ± 0.68	SF	×	...	×
284032	16:02:50.886	32:08:41.391	0.0141	9.49	6.92 ± 0.68	Composite	×	...	×
286477	15:48:36.238	36:13:42.486	0.0396	9.46	6.89 ± 0.68	SF	×	...	×
295794	11:36:57.683	41:13:18.507	0.0715	9.75	7.25 ± 0.68	Seyfert	✓	6.51	×
301231	13:18:29.733	45:17:01.821	0.0358	9.67	7.15 ± 0.68	Composite	×	...	×
301767	13:35:42.788	45:55:46.505	0.0048	8.95	6.26 ± 0.68	SF	×	...	✓
315748	08:02:13.476	22:26:02.457	0.03	9.28	6.66 ± 0.68	SF	×	...	×
316044	08:19:50.791	24:47:16.158	0.0256	9.65	7.12 ± 0.68	SF	×	...	×
319190	09:54:57.968	36:05:50.942	0.0488	9.39	6.8 ± 0.68	SF	×	...	×
321176	10:43:26.474	11:05:24.227	0.0475	9.64	7.12 ± 0.68	Seyfert	✓	8.163	✓
323877	11:46:04.072	11:34:52.566	0.0099	9.18	6.54 ± 0.68	SF	×	...	×
323951	11:48:32.458	12:42:19.067	0.0146	9.52	6.96 ± 0.68	SF	×	...	×
340153	14:38:58.286	47:18:28.497	0.027	9.66	7.14 ± 0.68	SF	×	...	×
346014	13:09:15.702	13:23:08.333	0.0274	9.23	6.61 ± 0.68	Composite	×	...	×

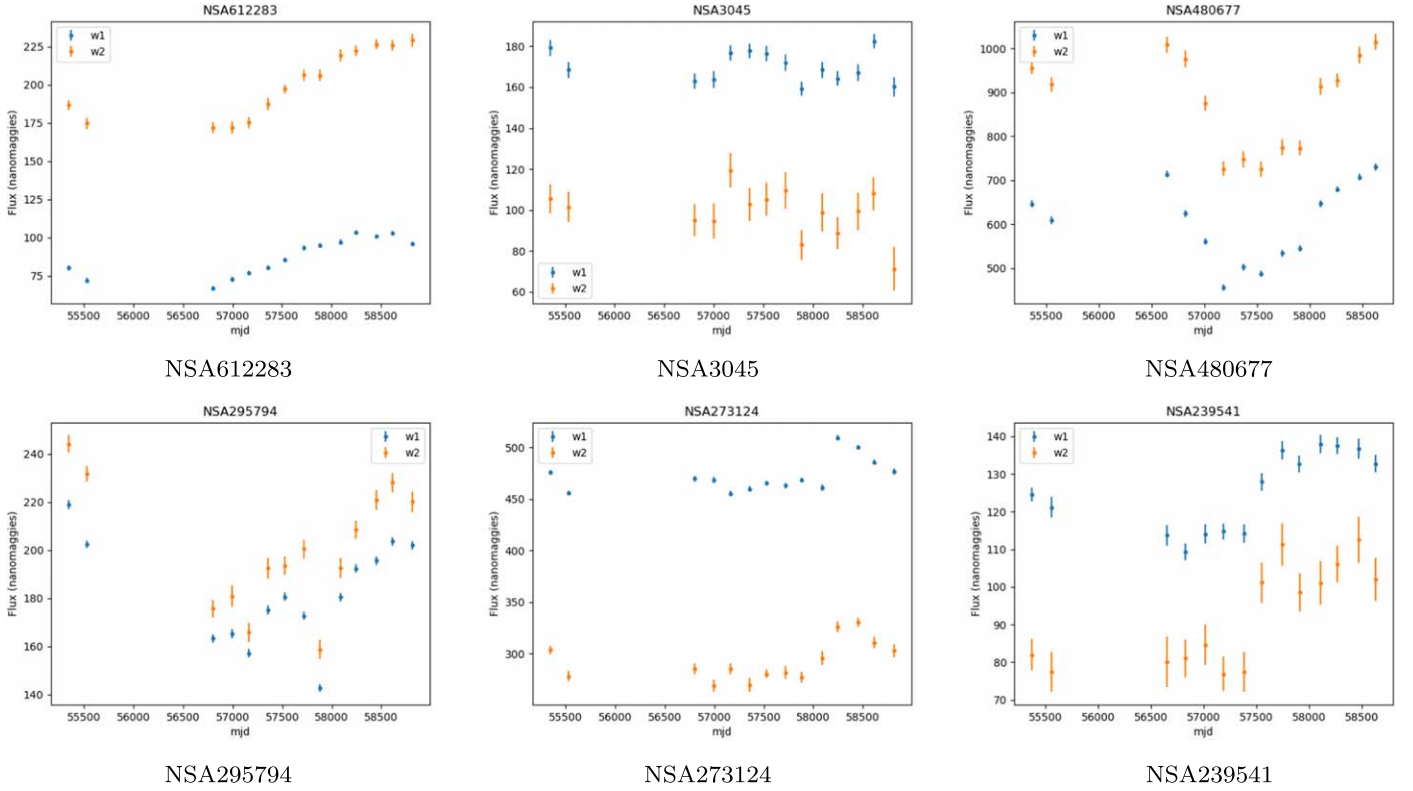
Table 4
(Continued)

NSA ID	R.A. (hms)	Decl. (dms)	z	$\log_{10}M_*(M_{\odot})$	$\log_{10}M_{\text{BH}}(M_{\odot})$	BPT Class	BLR?	$\log_{10}M_{\text{BH,vir}}(M_{\odot})$	Optical Var.?
354455	15:17:39.678	11:34:59.736	0.0652	9.5	6.94 ± 0.68	Composite	×	...	×
355963	15:43:58.996	08:07:34.691	0.0409	9.62	7.09 ± 0.68	SF	×	...	×
358934	07:44:02.155	45:30:20.646	0.0538	9.32	6.72 ± 0.68	SF	×	...	×
361340	10:07:10.915	12:39:06.079	0.0093	8.47	5.67 ± 0.68	SF	×	...	×
369885	13:07:33.823	14:00:31.128	0.0549	9.72	7.21 ± 0.68	SF	×	...	×
369924	13:07:17.443	13:38:47.968	0.0268	9.66	7.14 ± 0.68	Composite	×	...	×
370005	13:06:056.11	14:48:26.805	0.0032	8.1	5.21 ± 0.68	SF	×	...	×
370204	13:17:40.461	13:56:24.681	0.0283	9.01	6.34 ± 0.68	SF	×	...	×
376082	12:51:55.683	08:52:41.595	0.0038	8.45	5.63 ± 0.68	SF	×	...	×
376210	12:51:47.278	09:51:34.461	0.0305	9.27	6.66 ± 0.68	SF	×	...	×
376231	12:54:07.922	10:00:23.692	0.037	9.51	6.95 ± 0.68	Composite	×	...	×
376574	12:56:53.446	08:09:41.682	0.0086	8.75	6.0 ± 0.68	SF	×	...	×
376622	12:58:21.864	08:32:29.792	0.0289	9.56	7.01 ± 0.68	SF	×	...	×
377912	13:08:28.602	10:40:08.594	0.0246	9.68	7.16 ± 0.68	SF	×	...	×
385012	15:12:02.597	06:55:53.926	0.0465	9.73	7.23 ± 0.68	SF	×	...	×
385214	15:06:52.734	08:10:23.682	0.0396	9.24	6.62 ± 0.68	SF	×	...	×
386591	15:26:37.364	06:59:41.726	0.0384	9.39	6.8 ± 0.68	Composite	✓	5.485	×
389406	14:25:52.842	06:32:15.001	0.024	9.21	6.57 ± 0.68	SF	×	...	×
391212	15:04:16.147	05:49:21.806	0.0301	9.69	7.18 ± 0.68	SF	×	...	×
393092	16:03:43.582	04:32:35.996	0.0444	9.69	7.17 ± 0.68	SF	×	...	×
401713	08:02:53.694	55:17:55.692	0.03	9.41	6.83 ± 0.68	SF	×	...	×
404064	09:34:38.578	67:22:29.017	0.023	8.89	6.18 ± 0.68	SF	×	...	×
412056	09:46:23.749	34:16:52.073	0.0755	9.01	6.34 ± 0.68	SF	×	...	×
418509	13:34:05.899	27:33:40.195	0.0293	9.5	6.94 ± 0.68	Composite	×	...	×
418517	13:35:26.025	28:10:12.928	0.0633	9.63	7.1 ± 0.68	SF	×	...	×
418760	13:35:51.276	29:12:49.882	0.0212	9.17	6.53 ± 0.68	SF	×	...	×
418763	13:35:35.715	29:13:03.022	0.0028	8.19	5.32 ± 0.68	SF	×	...	×
424989	13:21:18.974	30:04:23.853	0.0912	9.66	7.14 ± 0.68	SF	✓	6.436	✓
431557	13:42:05.443	32:01:043.28	0.0156	9.46	6.89 ± 0.68	SF	×	...	×
437426	09:09:34.371	25:13:022.76	0.0078	8.98	6.29 ± 0.68	Composite	×	...	×
437561	09:17:17.051	26:26:59.206	0.0247	9.56	7.01 ± 0.68	SF	×	...	×
438165	12:03:25.676	33:08:46.147	0.0349	9.1	6.45 ± 0.68	SF	×	...	×
439902	13:39:57.611	30:42:54.223	0.042	9.65	7.12 ± 0.68	SF	×	...	×
439931	13:41:13.598	30:23:27.794	0.04	9.47	6.9 ± 0.68	SF	×	...	×
439935	13:42:43.255	30:43:39.805	0.0357	9.73	7.22 ± 0.68	Composite	×	...	×
439946	13:41:50.188	30:33:57.114	0.0264	9.11	6.46 ± 0.68	SF	×	...	✓
445385	13:28:24.676	31:09:37.833	0.0164	8.63	5.86 ± 0.68	...	×	...	×
451469	14:14:05.019	26:33:36.804	0.0358	9.66	7.14 ± 0.68	SF	✓	6.303	✓
453882	14:28:30.841	27:15:57.271	0.013	9.35	6.76 ± 0.68	SF	×	...	×
457334	14:47:17.407	24:30:19.296	0.0424	9.46	6.89 ± 0.68	SF	×	...	×
465843	15:46:53.324	17:52:21.579	0.0113	8.86	6.15 ± 0.68	SF	×	...	×
475108	11:30:26.846	30:27:52.084	0.0589	9.66	7.14 ± 0.68	Composite	×	...	×
475368	11:28:28.072	27:54:07.612	0.068	9.62	7.09 ± 0.68	Composite	×	...	×
477209	11:56:35.312	28:29:25.256	0.0117	9.28	6.67 ± 0.68	Composite	×	...	×
480677	12:29:03.509	29:46:45.995	0.0814	9.71	7.2 ± 0.68	SF	✓	...	✓
481291	12:36:012.26	26:45:22.078	0.0246	9.71	7.2 ± 0.68	SF	×	...	×
484296	13:29:39.134	25:47:50.822	0.0247	9.13	6.48 ± 0.68	SF	×	...	×
485578	08:04:18.001	15:20:038.47	0.0393	9.73	7.22 ± 0.68	Seyfert	×	...	×
487099	08:25:21.331	15:17:023.31	0.0329	9.49	6.93 ± 0.68	SF	×	...	×
487207	08:20:13.444	16:12:41.858	0.0442	9.56	7.01 ± 0.68	SF	×	...	×
488733	08:41:028.47	16:16:43.165	0.0731	9.72	7.21 ± 0.68	SF	×	...	×
501377	10:32:06.026	22:59:21.809	0.0585	8.97	6.29 ± 0.68	Composite	×	...	×
502687	10:05:0023.1	19:16:18.857	0.0128	8.73	5.98 ± 0.68	SF	×	...	×
508645	09:02:50.471	14:14:08.301	0.0506	9.48	6.92 ± 0.68	...	×	...	✓
522620	11:42:50.986	20:26:31.655	0.019	9.61	7.08 ± 0.68	SF	×	...	×
538951	12:32:36.165	18:01:23.085	0.0028	8.67	5.91 ± 0.68	SF	×	...	×
540489	13:13:54.174	16:43:39.707	0.0224	9.5	6.94 ± 0.68	SF	×	...	×
540494	13:13:40.008	16:39:27.698	0.0219	8.98	6.3 ± 0.68	SF	×	...	×
548558	13:13:050.79	23:15:17.935	0.0116	8.97	6.28 ± 0.68	SF	×	...	×
548726	13:23:016.62	21:18:005.97	0.0224	9.61	7.08 ± 0.68	Composite	×	...	×
548780	13:20:42.199	20:54:37.122	0.0093	8.44	5.63 ± 0.68	SF	×	...	×
552294	13:27:59.639	23:35:50.831	0.0432	9.32	6.72 ± 0.68	SF	×	...	×
558933	14:09:28.215	17:39:43.879	0.0181	9.67	7.15 ± 0.68	SF	×	...	×
563981	14:13:13.548	20:25:25.781	0.0168	9.52	6.97 ± 0.68	SF	×	...	×

Table 4
(Continued)

NSA ID	R.A. (hms)	Decl. (dms)	z	$\log_{10}M_*$ (M_\odot)	$\log_{10}M_{\text{BH}}$ (M_\odot)	BPT Class	BLR?	$\log_{10}M_{\text{BH,vir}}$ (M_\odot)	Optical Var.?
571135	15:10:24.257	19:23:47.709	0.075	9.56	7.01 ± 0.68	SF	×	...	×
572805	12:25:18.255	05:44:31.206	0.0038	9.11	6.46 ± 0.68	SF	×	...	×
576634	15:40:29.285	00:54:37.064	0.0117	8.59	5.81 ± 0.68	SF	×	...	×
583865	00:56:33.363	00:05:010.27	0.0793	9.45	6.88 ± 0.68	Seyfert	✓	6.131	×
592732	09:31:018.44	02:46:052.34	0.1148	8.83	6.11 ± 0.68	Composite	×	...	×
593159	11:04:16.043	05:16:30.756	0.1166	9.33	6.73 ± 0.68	Composite	×	...	×
600245	11:51:42.585	06:51:30.529	0.102	9.18	6.55 ± 0.68	Composite	×	...	×
612283	12:05:03.537	45:51:51.056	0.0654	7.52	4.48 ± 0.68	SF	×	...	×
627704	12:03:49.742	29:42:56.153	0.0105	9.46	6.89 ± 0.68	SF	×	...	×
638093	23:32:45.037	00:58:45.886	0.0238	9.45	6.88 ± 0.68	SF	×	...	×
648447	09:24:039.36	17:39:47.977	0.0136	9.6	7.06 ± 0.68	Composite	×	...	×
661360	11:33:23.454	55:04:20.733	0.0079	8.79	6.06 ± 0.68	SF	×	...	✓
676393	13:36:20.429	28:47:50.676	0.0268	9.51	6.95 ± 0.68	Composite	×	...	×
677377	13:46:22.893	29:19:02.782	0.0546	9.66	7.14 ± 0.68	SF	×	...	×
679695	14:07:24.993	55:06:10.896	0.0046	9.22	6.6 ± 0.68	Composite	×	...	×
681375	14:27:09.515	30:56:53.601	0.0137	9.59	7.06 ± 0.68	Composite	×	...	×
681956	14:34:037.05	59:20:018.29	0.0064	9.03	6.35 ± 0.68	SF	×	...	×
683356	14:48:27.022	31:47:28.383	0.0096	9.34	6.74 ± 0.68	SF	×	...	×
693966	12:59:20.083	09:11:13.787	0.0279	9.66	7.14 ± 0.68	Composite	×	...	×
694183	13:13:24.659	08:02:24.125	0.0237	9.71	7.2 ± 0.68	Composite	×	...	×

Note. Properties of the 148 AGN candidates with significant and correlated W1 and W2 variability found in forward-modeled WISE light curves. The IDs, positions, redshifts, and host galaxy stellar masses are those from the NSA catalog version $v_{1.0.1}$. In the $\log_{10}M_{\text{BH}}$ column we show the estimated BH mass based on the $M_* - M_{\text{BH}}$ relation from Schutte et al. (2019), which has a scatter of 0.68 dex. The presence of Balmer broad lines is indicated in the BLR column. Virial masses were calculated for broad-line AGN by Ho & Kim (2015) based on the width of the $H\alpha$ broad lines. *The estimated mass provided for NSA64525 by the NASA-Sloan Atlas ($10^{5.12} M_\odot$) is inconsistent with the stellar dispersion velocity of $193 \pm 8 \text{ km s}^{-1}$ measured by the SDSS spectroscopic pipeline. This σ_* is more characteristic of a host galaxy with mass $\sim 10^{9.5} M_\odot$ and a BH with mass $\sim 10^7 M_\odot$. In the last column, we indicate whether the WISE candidate's ZTF light curve also met the criteria for optical variability.

**Figure 7.** Six examples of WISE forward-modeling light curves that passed the variability criteria and were classified as IMBH candidates.

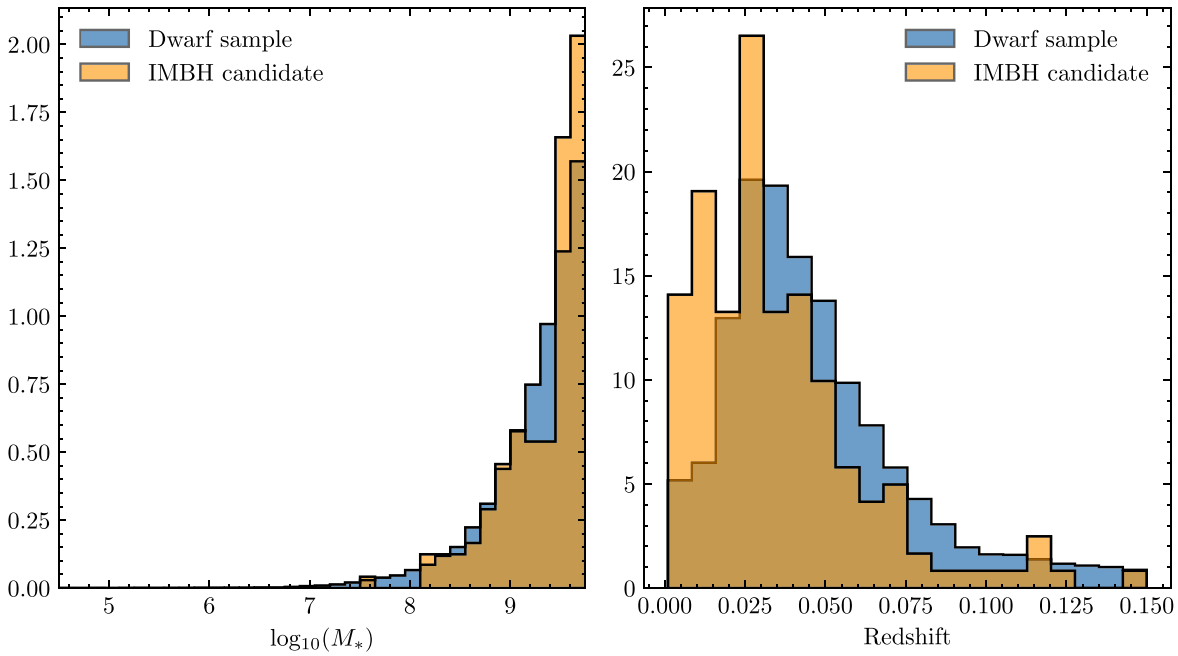


Figure 8. Normalized galaxy mass and redshift distributions of WISE IMBH candidates shown in green and the parent dwarf galaxy sample shown in blue. Redshifts and host galaxy mass measurements are derived from the NSA.

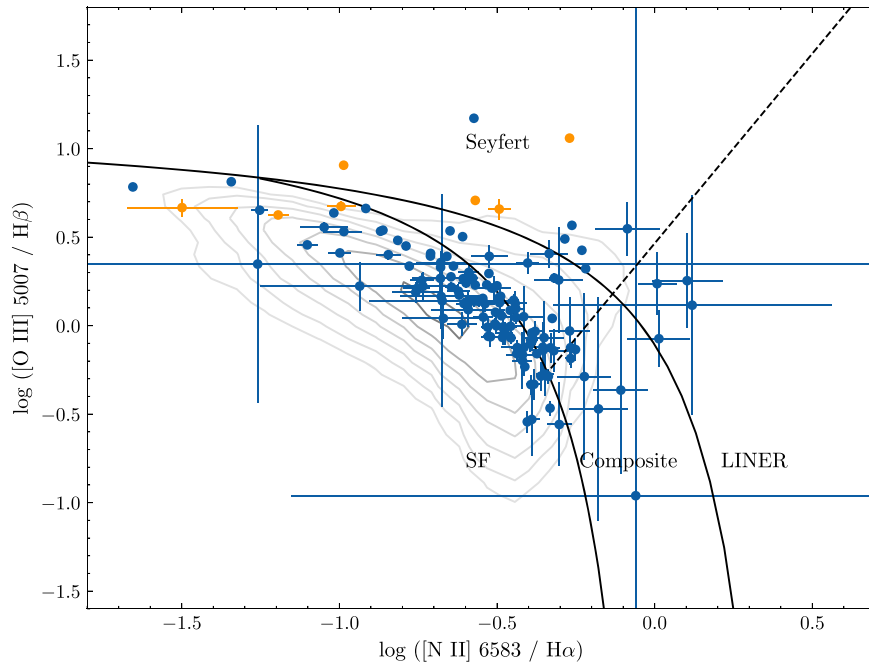


Figure 9. BPT diagram showing narrow line ratios derived from p_{PXF} fitting of archival SDSS spectra of the WISE-selected IMBH candidates. Orange points show line ratios for IMBH candidates with broad Balmer lines in archival spectra, and blue points show those with narrow emission lines only. Gray contours show the population density with log scaling of the entire parent dwarf galaxy sample for line ratios derived from the NASA-Sloan Atlas. Classification regions are labeled in black text.

sources (NSA164884 and NSA451469) were found in the original ZTF sample, due to the smaller sample of dwarf galaxies for which we produced optical photometry. The AGN with both mid-IR and optical variability are indicated in the last column of Table 4.

NSA451469 had also been found in PTF by Baldassare et al. (2020b). We cross-matched our mid-IR-selected IMBH candidates to the active dwarf galaxies from the Secrest & Satyapal (2020) mid-IR variability search, the Baldassare et al. (2018, 2020b) optical variability searches, the Molina et al.

(2021) [Fe x] λ 6374 coronal line emission search, the Mezcua & Domínguez Sánchez (2020) IFU spectroscopy search, the Mezcua et al. (2018) Chandra X-ray search, the Latimer et al. (2021) mid-IR color selection box search, and the Reines et al. (2013) optical emission-line search. Only two objects had been found in previous AGN searches.

One object, NSA638093, had previously been found in the WISE variability search by Secrest & Satyapal (2020) and in the mid-IR color selection box by Latimer et al. (2021) (object number 11, listed with NSAID 151888 from version v_{1-1-2} of

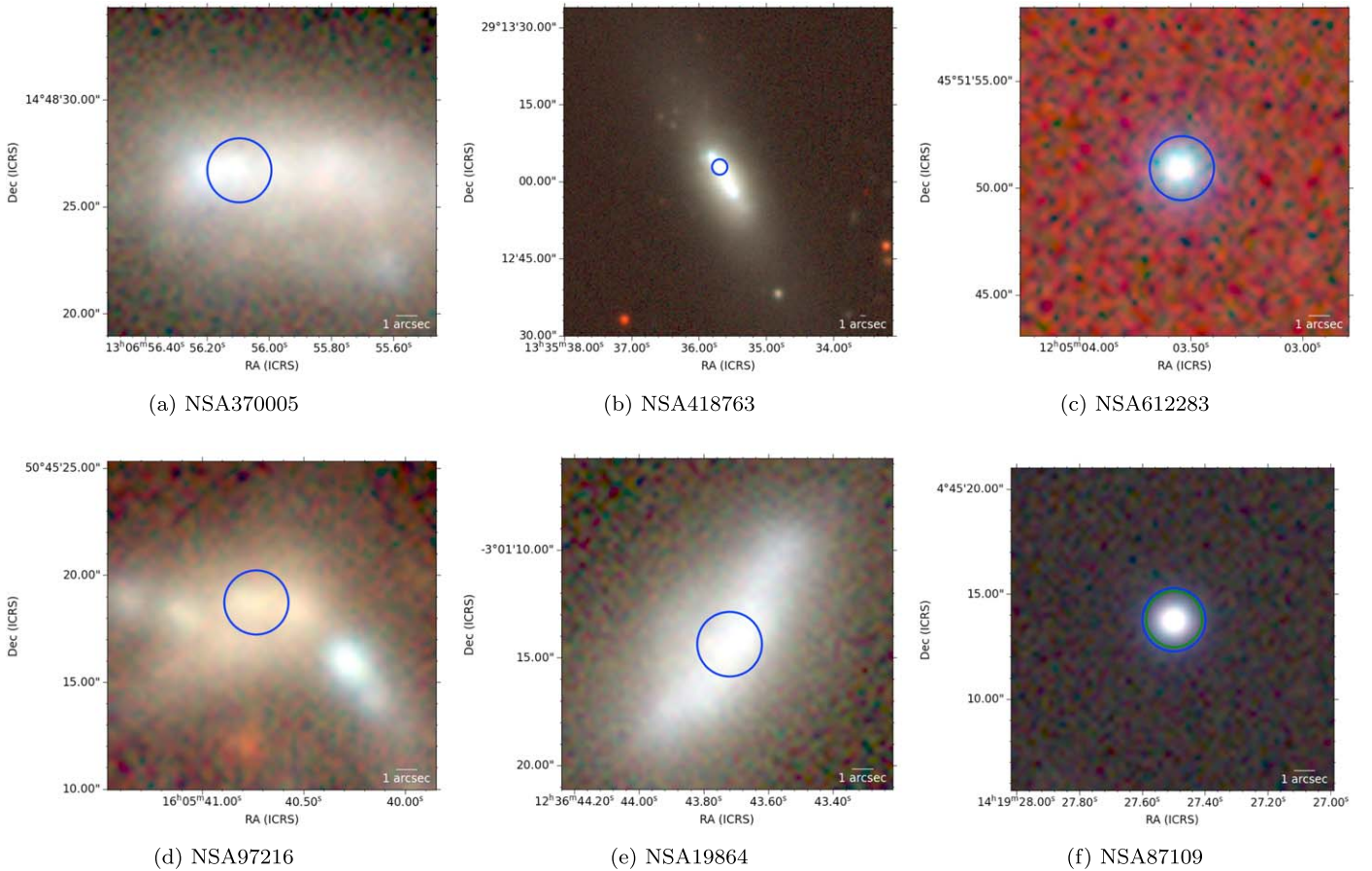


Figure 10. Legacy survey cutouts of three WISE IMBH candidates (panels (a)–(c)) and two ZTF IMBH candidates (panels (d)–(e)) with host masses $M_* < 10^{8.2} M_\odot$ and the candidate with a FIRST radio detection (panel (f)), radio position overlaid with a green circle. Blue circles show the central position for WISE or ZTF forced photometry.

the NSA), where they used Chandra to find X-ray emission that may have been consistent with X-ray binaries instead of AGN activity. NSA386591 appears in the Reines et al. (2013) spectroscopic search for BPT AGN and composites and the Latimer et al. (2021) mid-IR color selection search (ID number 6), where it was found to have an X-ray luminosity consistent with AGN activity and too large to be produced by X-ray binaries.

We undertook a search for radio emission from the IMBH candidates in the Karl G. Jansky Very Large Array Sky Survey (VLASS; Lacy et al. 2020). This survey covers a total of $33,885 \text{ deg}^2$ in the 2–4 GHz range with an angular resolution of $\sim 2''$ and will obtain a co-add 1σ sensitivity of $1 \mu\text{Jy beam}^{-1}$ by survey end in 2024. We searched for cross-matches within $10''$ in Table 2 of the VLASS Epoch 1 Quick Look Catalogue, which contains $\approx 700,000$ compact radio sources with $> 1 \text{ mJy beam}^{-1}$ detections associated with mid-IR hosts from the unWISE catalog (Gordon et al. 2020). We found that one IMBH candidate, NSA87109, had a corresponding radio point source at a separation of $0''.0038$ from the optical NASA-Sloan Atlas galaxy position with a flux of $17.55 \pm 0.27 \text{ Jy}$. This object is a known BL Lac that has also been detected in 0.1–2.4 keV X-rays (Massaro et al. 2009)

We show cutouts from the DESI Legacy Imaging Surveys (Dey et al. 2019) of three WISE candidates and two ZTF candidates with host masses $M_* < 10^{8.2} M_\odot$ and the object with a VLASS radio detection (NSA87109, with stellar mass $\log_{10} M_* = 9.66$) in Figure 10. The radio source and one other

low-mass IMBH candidate are in compact, blue galaxies, while the other four low-mass IMBH candidates reside in galaxies with complex morphologies and multiple stellar overdensities.

9. Discussion

The number of dwarf galaxies that were variable in WISE corresponded to a $0.19\% \pm 0.02\%$ variability fraction, while the optical variability fraction that we find from the ZTF AGN candidates is $0.17\% \pm 0.03\%$. Our results therefore suggest that the two methods are similarly effective for identifying IMBH candidates with the current sensitivities and baselines available for mid-IR and optical photometry of dwarf galaxies. This, however, will change with the improved optical sensitivities and baselines offered by the LSST survey over the next decade.

Our mid-IR active fraction was larger but within the uncertainty range of the active fraction found by Secrest & Satyapal (2020; $0.09^{+0.20}_{-0.07}\%$) in a much smaller sample of 2197 dwarf galaxies with the main WISE photometry catalog. The optical variability fraction that we find is also consistent with the active fraction of $0.15\% \pm 0.07\%$ found for dwarf galaxies of the same mass in PTF (Baldassare et al. 2020b).

The 90% fraction of WISE-selected AGN candidates that are variable in the mid-IR but not the optical likely arises from a combination of line-of-sight obscuration of nuclear optical emission due to the dusty torus and global obscuration from the host galaxy. Obscuration of nuclear optical emission from AGN with detectable mid-IR signatures has been observed for

many Seyfert 2 galaxies (e.g., Goulding et al. 2011; Annuar et al. 2015; Ricci et al. 2016; Annuar et al. 2017). It is possible that the majority of our mid-IR variable AGN in dwarf galaxies are Seyfert 2 galaxies with obscured optical variability that are also not picked up by the BPT diagram owing to the effects of their lower masses on the optical emission-line ratios. Line-of-sight obscuration of optical emission of WISE candidates is supported by the fact that 7 of the 12 WISE-selected IMBH candidates with bright BLRs were variable in both the mid-IR and the optical.

We note that only 5 of the 152 dwarf galaxies in common with the Baldassare et al. (2020b) AGN candidate sample from PTF were variable in ZTF. This may be because of the use of differing statistical criteria for variability classification. It may also be the case that the longer 7 yr baseline of the combined PTF and iPTF light curves in Baldassare et al. (2020b) improved their sensitivity to AGN that vary on longer timescales compared to shorter timescales. They indeed find that longer-baseline data have a much higher detectable variability fraction, increasing by a factor of 4 from 0.25% for light curves with <2 yr baselines to 1% for light curves with >2 yr baselines. By comparison, our procedure of using deep references and stacking to detect fainter variability in more evenly sampled, ~ 3 yr baseline light curves may make us more sensitive to variability on month-to-year-long timescales but may miss AGN with flux changes over longer 2–7 yr timescales. An alternative explanation may be that a large fraction of low-mass AGN are state-changing AGN (e.g., Frederick et al. 2019) that can switch their optical variability on and off over the decade-long timescale of the PTF and ZTF surveys. Indeed, Martínez-Palomera et al. (2020) found that the majority of IMBH candidates with optical variability on hourly to daily timescales from the SIBLING survey were not variable when observed again the following year.

A total of 81% of the ZTF-selected IMBH candidates were star-forming on the BPT diagram, and only seven have been identified as AGN via their Balmer broad lines. Only seven had been identified in previous dwarf galaxy AGN searches, and these were all via their optical variability in SDSS or PTF. The non-AGN spectroscopic classifications of the majority of the sources indicate that optical variability selection can find AGN in dwarf galaxies that would be missed by other selection strategies.

Similarly, 100 (69%) of the WISE-selected IMBH candidates were star-forming on the BPT diagram and therefore would have been missed by classic spectroscopic selection methods. A total of 12 (8.1%) can be identified as AGN owing to the presence of broad lines, 1 (0.63%) could have been found via radio emission alone, another 2 (1.27%) via the mid-IR selection box, and 1 (0.63%) via X-ray emission. We therefore see that $\sim 70\%$ of candidates from mid-IR variability selection could likely not have been found through other selection techniques. A higher fraction of the WISE-selected candidates are BPT AGN compared to optically selected candidates, perhaps indicating that the AGN emission lines of galaxies with mid-IR variability are less likely to be diluted by star formation.

Both the ZTF-selected and WISE-selected AGN candidate host galaxies tend to have higher masses and lower redshifts compared to the overall distributions of the host galaxy sample, likely due to the higher luminosities of these AGN. However, our selection method is still capable of detecting AGN

variability from dwarf galaxies with redshifts up to $z \sim 0.15$ and stellar masses down to $M_* = 10^{7.52} M_\odot$. The virial masses for the AGN candidates with broad lines go down to $M_{\text{BH}} = 10^{5.485} M_\odot$ and in most cases are lower than the BH masses estimated from the $M_{\text{BH}} - M_*$ relation, indicating that our search may have found MBHs that are undermassive for their hosts. We therefore conclude that our variability selection approach is useful for selecting AGN that can populate the poorly sampled lower end of the $M_{\text{BH}} - \sigma_*$ relation. Future work should take high-resolution spectra of our IMBH candidates for fitting of the velocity dispersion from the stellar absorption lines to provide another independent estimate of the BH mass.

The discovery of 36 nuclear SN candidates shows the usefulness of applying simple statistics to ZTF forced photometry of large galaxy samples to find SN candidates in dwarf galaxies. There are many motivations to study rates of SNe in dwarfs, such as explaining the increase in the rate ratio of superluminous SNe to core-collapse SNe in low-mass galaxies and whether the increased metallicity or specific star formation rates in dwarfs are the driving factor for this trend (Taggart & Perley 2021). It has also been found that the emerging class of fast blue optical transients like AT2018cow are preferentially hosted by dwarf galaxies (Perley et al. 2021). Our finding that 0.14% of dwarf galaxies contained nuclear SNe during ZTF Phase I (corresponding to $0.05\% \text{ yr}^{-1}$) and that most SNe were within redshifts of $0.02 < z < 0.055$ may provide insights into these questions.

10. Conclusions

In this paper we have presented a search for IMBH candidates by looking for variable AGN in dwarf galaxies of stellar mass $M_* < 10^{9.75} M_\odot$ in the optical and mid-IR. We applied a new ZTF forced photometry pipeline to produce deep, high-quality reference images for image subtraction and made g - and r -band light curves of 25,714 dwarf galaxies. These light curves were stacked in a range of time bins to improve sensitivity to faint variability. We applied statistical cutoffs to find significant and correlated variability between the two bands and found 36 SN candidates and 44 AGN candidates. The SN fraction was $0.05\% \pm 0.01\% \text{ yr}^{-1}$, and the optically variable AGN fraction was $0.17\% \pm 0.03\%$.

To search for mid-IR variability, we used Tractor forward-modeled photometry of time-resolved WISE co-adds. We found 148 dwarf galaxies with significant and correlated variability in the W1 and W2 bands after removing 14 SNe. The mid-IR variable AGN fraction was $0.19\% \pm 0.02\%$.

We found that 81% of our ZTF AGN candidates would have been missed with classical spectroscopic classification on the BPT diagram. Of our WISE candidates, 69% would have been missed with spectroscopic classification, and only four would have been detected via radio or X-ray detection or the mid-IR color selection box. While our candidates were slightly biased to low redshifts and high galaxy masses compared to the parent dwarf galaxy sample, they were effective in identifying AGN with virial masses as low as $M_{\text{BH}} = 10^{5.485} M_\odot$ and in dwarf galaxies with stellar masses $10^{7.5} M_\odot < M_* < 10^{8.5} M_\odot$. We therefore conclude, in accordance with previous variability searches, that optical and mid-IR variability selection is effective for finding low-mass AGN in dwarf galaxies that would be missed by other spectroscopic selection techniques.

After checking the ZTF photometry of the 152 dwarf galaxies in common between our parent sample and the

variability-selected AGN candidates from PTF (Baldassare et al. 2020b), we found that only five continue to show variability in ZTF. The lack of variability in our ZTF light curves may be due to the different baselines and sensitivities of the two search strategies and the differing methods for finding AGN-like variability.

With more detailed imaging and spectroscopic analysis, our variability-selected AGN candidates could help to populate the sparsely sampled end of the M_* - σ relation and provide insights into BH seed formation mechanisms, dwarf galaxy –BH coevolution, and the accretion states of low-mass AGN. Future work on these candidates will include forward modeling of ZTF and DECam images to determine their positions relative to their host galaxy nuclei and determine the off-nuclear fraction. The potential for forward modeling of ZTF images to determine the position of a variable point source relative to its host galaxy was demonstrated in Ward et al. (2021) for recoiling SMBH candidates and will provide a way to confirm the positions of IMBH candidates without X-ray or radio detections.

These candidates are just the tip of the iceberg in the search for optically variable AGN in dwarf galaxies, which will be greatly enhanced by the capabilities of the Legacy Survey of Space and Time (LSST) at Vera C. Rubin Observatory (Ivezic et al. 2019) over the next decade. The capacity of LSST to find fainter and more distant IMBHs in dwarf galaxies via their variability will tighten the constraints we can place on BH seeding channels and the efficiency of massive BH growth.

We thank the anonymous referee for their very helpful feedback, which has helped us to substantially improve the manuscript. The authors would also like to thank Yuhan Yao for her useful comments.





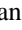
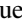
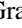
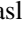

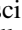

Based on observations obtained with the Samuel Oschin 48-inch Telescope and the 60-inch Telescope at the Palomar Observatory as part of the Zwicky Transient Facility project. ZTF is supported by the National Science Foundation under grant No. AST-2034437 and a collaboration including Caltech, IPAC, the Weizmann Institute for Science, the Oskar Klein Center at Stockholm University, the University of Maryland, Deutsches Elektronen-Synchrotron and Humboldt University, the TANGO Consortium of Taiwan, the University of Wisconsin at Milwaukee, Trinity College Dublin, Lawrence Livermore National Laboratories, and IN2P3, France. Operations are conducted by COO, IPAC, and UW. The ZTF forced photometry service was funded under the Heising-Simons Foundation grant 12540303 (PI: Graham). E.C.K. acknowledges support from the G.R.E.A.T. research environment funded by *Vetenskapsrådet*, the Swedish Research Council, under project No. 2016-06012, and support from The Wenner-Gren Foundations. M.M.K. acknowledges generous support from the David and Lucille Packard Foundation. This work was supported by the GROWTH project funded by the National Science Foundation under grant No. 1545949.

This research used resources of the National Energy Research Scientific Computing Center, a DOE Office of Science User Facility supported by the Office of Science of the U.S. Department of Energy under contract No. DE-AC02-05CH11231. P.E.N. acknowledges support from the DOE under grant DE-AC02-05CH11231, Analytical Modeling for Extreme-Scale Computing Environments.

This project used data obtained with the Dark Energy Camera (DECam), which was constructed by the Dark Energy Survey (DES) collaboration. Funding for the DES Projects has been provided by the U.S. Department of Energy, the U.S. National Science Foundation, the Ministry of Science and Education of Spain, the Science and Technology Facilities Council of the United Kingdom, the Higher Education Funding Council for England, the National Center for Supercomputing Applications at the University of Illinois at Urbana-Champaign, the Kavli Institute of Cosmological Physics at the University of Chicago, the Center for Cosmology and Astro-Particle Physics at The Ohio State University, the Mitchell Institute for Fundamental Physics and Astronomy at Texas A&M University, Financiadora de Estudos e Projetos, Fundacao Carlos Chagas Filho de Amparo, Financiadora de Estudos e Projetos, Fundacao Carlos Chagas Filho de Amparo a Pesquisa do Estado do Rio de Janeiro, Conselho Nacional de Desenvolvimento Cientifico e Tecnologico and the Ministerio da Ciencia, Tecnologia e Inovacao, the Deutsche Forschungsgemeinschaft, and the Collaborating Institutions in the Dark Energy Survey. The Collaborating Institutions are Argonne National Laboratory, the University of California at Santa Cruz, the University of Cambridge, Centro de Investigaciones Energeticas, Medioambientales y Tecnologicas-Madrid, the University of Chicago, University College London, the DES-Brazil Consortium, the University of Edinburgh, the Eidgenossische Technische Hochschule (ETH) Zurich, Fermi National Accelerator Laboratory, the University of Illinois at Urbana-Champaign, the Institut de Ciencies de l’Espai (IEEC/CSIC), the Institut de Fisica d’Altes Energies, Lawrence Berkeley National Laboratory, the Ludwig-Maximilians Universitat Munchen and the associated Excellence Cluster Universe, the University of Michigan, the National Optical Astronomy Observatory, the University of Nottingham, The Ohio State University, the University of Pennsylvania, the University of Portsmouth, SLAC National Accelerator Laboratory, Stanford University, the University of Sussex, and Texas A&M University.

Software: Ampel (Nordin et al. 2019), Astromatic (<https://www.astromatic.net/>), Astropy (Robitaille et al. 2013; Price-Whelan et al. 2018), catsHTM (Soumagnac & Ofek 2018), extcats (github.com/MatteoGiomi/extcats), GROWTH Marshal (Kasliwal et al. 2019), Hotpants (<https://github.com/acbecker/hotpants>), The Tractor (Lang et al. 2016a).

ORCID iDs

Charlotte Ward  <https://orcid.org/0000-0002-4557-6682>
 Suvi Gezari  <https://orcid.org/0000-0003-3703-5154>
 Peter Nugent  <https://orcid.org/0000-0002-3389-0586>
 Eric C. Bellm  <https://orcid.org/0000-0001-8018-5348>
 Richard Dekany  <https://orcid.org/0000-0002-5884-7867>
 Dmitry A. Duvvuri  <https://orcid.org/0000-0001-5060-8733>
 Matthew J. Graham  <https://orcid.org/0000-0002-3168-0139>
 Mansi M. Kasliwal  <https://orcid.org/0000-0002-5619-4938>
 Erik C. Kool  <https://orcid.org/0000-0002-7252-3877>
 Frank J. Masci  <https://orcid.org/0000-0002-8532-9395>
 Reed L. Riddle  <https://orcid.org/0000-0002-0387-370X>

References

- Anglés-Alcázar, D., Faucher-Giguère, C. A., Quataert, E., et al. 2017, *MNRAS*, 472, L109
 Annun, A., Alexander, D. M., Gandhi, P., et al. 2017, *ApJ*, 836, 165

- Annun, A., Gandhi, P., Alexander, D. M., et al. 2015, *ApJ*, **815**, 36
- Baldassare, V. F., Dickey, C., Geha, M., & Reines, A. E. 2020a, *ApJL*, **898**, L3
- Baldassare, V. F., Geha, M., & Greene, J. 2018, *ApJ*, **868**, 152
- Baldassare, V. F., Geha, M., & Greene, J. 2020b, *ApJ*, **896**, 10
- Baldwin, J. A., Phillips, M. M., & Terlevich, R. 1981, *PASP*, **93**, 5
- Bellm, E. C., Kulkarni, S. R., Barlow, T., et al. 2019a, *PASP*, **131**, 68003
- Bellm, E. C., Kulkarni, S. R., Graham, M. J., et al. 2019b, *PASP*, **131**, 018002
- Bellovary, J. M., Cleary, C. E., Munshi, F., et al. 2018, *MNRAS*, **482**, 2913
- Bellovary, J. M., Hayoune, S., Chafra, K., et al. 2021, *MNRAS*, **505**, 5129
- Blanton, M. R., Kazin, E., Muna, D., Weaver, B. A., & Price-Whelan, A. 2011, *AJ*, **142**, 31
- Blanton, M. R., & Roweis, S. 2007, *AJ*, **133**, 734
- Bohn, T., Canalizo, G., Veilleux, S., & Liu, W. 2021, *ApJ*, **911**, 70
- Borucki, W. J., Koch, D., Basri, G., et al. 2010, *Sci*, **327**, 977
- Bruzual, G., & Charlot, S. 2003, *MNRAS*, **344**, 1000
- Burke, C. J., Shen, Y., Blaes, O., et al. 2021, *Sci*, **373**, 789
- Burke, C. J., Shen, Y., Chen, Y.-C., et al. 2020, *ApJ*, **899**, 136
- Butler, N. R., & Bloom, J. S. 2011, *AJ*, **141**, 93
- Cann, J. M., Satyapal, S., Abel, N. P., et al. 2019, *ApJL*, **870**, L2
- Cappellari, M. 2016, *MNRAS*, **466**, 798
- Cappellari, M., & Emsellem, E. 2004, *PASP*, **116**, 138
- Chandra, P., Chevalier, R. A., Chugai, N., Fransson, C., & Soderberg, A. M. 2015, *ApJ*, **810**, 32
- Dekany, R., Smith, R. M., Riddle, R., et al. 2020, *PASP*, **132**, 038001
- Dey, A., Schlegel, D. J., Lang, D., et al. 2019, *AJ*, **157**, 168
- Dickey, C., Geha, M., Wetzel, A., & El-Badry, K. 2019, *ApJ*, **884**, 180
- Drake, A. J., Djorgovski, S. G., Graham, M. J., et al. 2019, *MNRAS*, **482**, 98
- Ferrarese, L., & Merritt, D. 2000, *ApJ*, **539**, L9
- Fransson, C., Ergon, M., Challis, P. J., et al. 2014, *ApJ*, **797**, 118
- Frederick, S., Gezari, S., Graham, M. J., et al. 2019, *ApJ*, **883**, 31
- Geha, M., Blanton, M. R., Yan, R., & Tinker, J. L. 2012, *ApJ*, **757**, 85
- Gordon, Y. A., Boyce, M. M., O'Dea, C. P., et al. 2020, *RNAAS*, **4**, 175
- Goulding, A. D., Alexander, D. M., Mullaney, J. R., et al. 2011, *MNRAS*, **411**, 1231
- Graham, M. J., Kulkarni, S. R., Bellm, E. C., et al. 2019, *PASP*, **131**, 078001
- Greene, J. E., Strader, J., & Ho, L. C. 2020, *ARA&A*, **58**, 257
- Habouzit, M., Volonteri, M., & Dubois, Y. 2017, *MNRAS*, **468**, 3935
- Ho, L. C., & Kim, M. 2015, *ApJ*, **809**, 123
- Holley-Bockelmann, K., Gültekin, K., Shoemaker, D., & Yunes, N. 2008, *ApJ*, **686**, 829
- Ivezić, v., Kahn, S. M., Tyson, J. A., et al. 2019, *ApJ*, **873**, 111
- Kasliwal, M. M., Cannella, C., Bagdasaryan, A., et al. 2019, *PASP*, **131**, 038003
- Kelly, B. C., Bechtold, J., & Siemiginowska, A. 2009, *ApJ*, **698**, 895
- Kormendy, J., & Ho, L. C. 2013, *ARA&A*, **51**, 511
- Koudmani, S., Sijacki, D., Bourne, M. A., & Smith, M. C. 2019, *MNRAS*, **484**, 2047
- Kristensen, M. T., Pimblett, K., Gibson, B., Penny, S., & Koudmani, S. 2021, *ApJ*, **922**, 127
- Lacy, M., Baum, S. A., Chandler, C. J., et al. 2020, *PASP*, **132**, 035001
- Lang, D. 2014, *AJ*, **147**, 108
- Lang, D., Hogg, D. W., & Mykytyn, D. 2016a, The Tractor: Probabilistic astronomical source detection and measurement, Astrophysics Source Code Library, ascl:1604.008
- Lang, D., Hogg, D. W., & Schlegel, D. J. 2016b, *AJ*, **151**, 36
- Latimer, C. J., Reines, A. E., Hainline, K. N., Greene, J. E., & Stern, D. 2021, *ApJ*, **914**, 133
- Law, N. M., Kulkarni, S. R., Dekany, R. G., et al. 2009, *PASP*, **121**, 1395
- Liu, H.-Y., Liu, W.-J., Dong, X.-B., et al. 2019, *ApJS*, **243**, 21
- Liu, W., Veilleux, S., Canalizo, G., et al. 2020, *ApJ*, **905**, 166
- MacLeod, C. L., Brooks, K., Ivezić, Ž., et al. 2011, *ApJ*, **728**, 26
- Mainzer, A., Bauer, J., Cutri, R. M., et al. 2014, *ApJ*, **792**, 30
- Mainzer, A., Bauer, J., Grav, T., et al. 2011, *ApJ*, **731**, 53
- Martínez-Palomera, J., Lira, P., Bhalla-Ladd, I., Förster, F., & Plotkin, R. M. 2020, *ApJ*, **889**, 113
- Masci, F. J., Laher, R. R., Rusholme, B., et al. 2019, *PASP*, **131**, 018003
- Massaro, E., Giommi, P., Leto, C., et al. 2009, *A&A*, **495**, 691
- Meisner, A. M., Lang, D., & Schlegel, D. J. 2017, *AJ*, **154**, 161
- Meisner, A. M., Lang, D., & Schlegel, D. J. 2018, *AJ*, **156**, 69
- Mezcua, M., Civano, F., Marchesi, S., et al. 2018, *MNRAS*, **478**, 2576
- Mezcua, M., & Domínguez Sánchez, H. 2020, *ApJL*, **898**, L30
- Miller, M. C., & Hamilton, D. P. 2002, *MNRAS*, **330**, 232
- Molina, M., Reines, A. E., Latimer, C. J., Baldassare, V., & Salehirad, S. 2021, *ApJ*, **922**, 155
- Nordin, J., Brinell, V., van Santen, J., et al. 2019, *A&A*, **631**, A147
- Pacucci, F., Loeb, A., Mezcua, M., & Martín-Navarro, I. 2018, *ApJL*, **864**, L6
- Pacucci, F., Mezcua, M., & Regan, J. A. 2021, *ApJ*, **920**, 134
- Patterson, M. T., Bellm, E. C., Rusholme, B., et al. 2019, *PASP*, **131**, 18001
- Penny, S. J., Masters, K. L., Smethurst, R., et al. 2018, *MNRAS*, **476**, 979
- Perley, D. A., Ho, A. Y. Q., Yao, Y., et al. 2021, *MNRAS*, **508**, 5138
- Polimera, M., Sarajedini, V., Ashby, M. L., Willner, S. P., & Fazio, G. G. 2018, *MNRAS*, **476**, 1111
- Portegies Zwart, S. F., & McMillan, S. L. W. 2002, *ApJ*, **576**, 899
- Price-Whelan, A. M., Sipőcz, B. M., Günther, H. M., et al. 2018, *AJ*, **156**, 123
- Reines, A. E., & Comastri, A. 2016, *PASA*, **33**, e054
- Reines, A. E., Condon, J. J., Darling, J., & Greene, J. E. 2020, *ApJ*, **888**, 36
- Reines, A. E., Greene, J. E., & Geha, M. 2013, *ApJ*, **775**, 116
- Ricarte, A., & Natarajan, P. 2018, *MNRAS*, **481**, 3278
- Ricarte, A., Tremmel, M., Natarajan, P., Zimmer, C., & Quinn, T. 2021, *MNRAS*, **503**, 6098
- Ricci, C., Bauer, F. E., Treister, E., et al. 2016, *ApJ*, **819**, 4
- Robitaille, T. P., Tollerud, E. J., Greenfield, P., et al. 2013, *A&A*, **558**, A33
- Sánchez, P., Lira, P., Cartier, R., et al. 2017, *ApJ*, **849**, 110
- Schutte, Z., Reines, A. E., & Greene, J. E. 2019, *ApJ*, **887**, 245
- Secrest, N. J., & Satyapal, S. 2020, *ApJ*, **900**, 56
- Sharma, R., Brooks, A., Somerville, R. S., et al. 2019, *ApJ*, **897**, 103
- Shaya, E. J., Olling, R., & Mushotzky, R. 2015, *AJ*, **150**, 188
- Smitka, M. T. 2016, PhD thesis, Texas A&M Univ.
- Soumagnac, M. T., & Ofek, E. O. 2018, *PASP*, **130**, 075002
- Stoll, R., Prieto, J. L., Stanek, K. Z., et al. 2011, *ApJ*, **730**, 34
- Taggart, K., & Perley, D. A. 2021, *MNRAS*, **503**, 3931
- Veilleux, S., & Osterbrock, D. E. 1987, *ApJS*, **63**, 295
- Volonteri, M., & Begelman, M. C. 2010, *MNRAS*, **409**, 1022
- Volonteri, M., & Natarajan, P. 2009, *MNRAS*, **400**, 1911
- Volonteri, M., & Perna, R. 2005, *MNRAS*, **358**, 913
- Volonteri, M., & Reines, A. E. 2016, *ApJL*, **820**, L6
- Ward, C., Gezari, S., Frederick, S., et al. 2021, *ApJ*, **913**, 102
- Woo, J.-H., Schulze, A., Park, D., et al. 2013, *ApJ*, **772**, 49
- Wright, E. L., Eisenhardt, P. R., Mainzer, A. K., et al. 2010, *AJ*, **140**, 1868